

Quasi-static analysis of planar sliding using friction patches

The International Journal of
Robotics Research
2020, Vol. 39(14) 1775–1795
© The Author(s) 2020
Article reuse guidelines:
sagepub.com/journals-permissions
DOI: 10.1177/0278364920929082
journals.sagepub.com/home/ijr



M. Mahdi Ghazaei Ardakani¹ , Joao Bimbo¹ and Domenico Prattichizzo^{1,2}

Abstract

Flat objects lying on a surface are hard to grasp, but could be manipulated by sliding along the surface in a non-prehensile manner. This strategy is commonly employed by humans as pre-manipulation, for example to bring a cell phone to the edge of a table to pick it up. To endow robots with a similar capability, we introduce a mathematical model of planar sliding by means of a soft finger. The model reveals various aspects of interaction through frictional contacts, which can be used for planning and control. Specifically, using a quasi-static analysis we are able to derive a hybrid dynamical system to predict the motion of the object and the interaction forces. The conditions for which the object sticks to the friction patch, pivots, or completely slides against it are obtained. It is possible to find fixed points of the system and the path taken by the object to reach such configurations. Theoretical as well as comprehensive experimental results are presented.

Keywords

Planar sliding, non-prehensile manipulation, soft finger, frictional contact

1. Introduction

Objects can be manipulated using either a prehensile or a non-prehensile approach. Thin flat objects on a surface are difficult to grasp, but can be manipulated by pushing or pulling. Several strategies are imaginable, such as caging the object within the hand, if the object is small compared with a hand. Depending on the height of the object, it could also be pushed from the side by some parts of the hand or moved by using an elevated edge or any bumps or dents on its surface. In certain cases, force closure can be achieved by, for example, pressing the object against the table and moving the object as if it was grasped. Nevertheless, a practically interesting case is when the hand is placed on top of the object, but the friction between the object and the hand is controlled such that the object can pivot (Figure 1). This strategy is an example of exploiting environmental constraints for manipulation (Malvezzi et al., 2019). The benefits are immediate when force closure is impossible, no matter how hard the object is pressed (e.g., due to a small contact area), or when hand reorientation is limited, for example due to kinematic limitations of the robotic arm.

When a robot end-effector (e.g., a hand or a soft finger) establishes a frictional contact with an object, it can transfer forces through the friction patch formed between them. This contact, when used for pivoting, behaves similarly to a joint. However, it can transfer not only forces between the end-effector and the object but also torque. This fact can be used to control the angular velocity of the object.

Contact mechanics is a complex phenomenon (Johnson, 1985). Howe et al. (1988) studied the contact between robot fingers and the surface of an object under combined torsion and shear loading for the prediction of the initiation of the slippage. The concept of limit surfaces (LS) has been introduced as a convenient way to characterize the friction properties of two surfaces sliding against each other (Goyal, 1989). A practical approximation of the LS was proposed by Howe and Cutkosky (1996). The observation is that LSs can be approximated by ellipsoids. The ellipsoidal approximation has been widely studied for making realistic models for soft fingers in robotics (Bicchi et al., 1993; Fakhari et al., 2016; Xydias and Kao, 1999). In this work, we have utilized the ellipsoid approximation of LSs for modeling the friction between the soft finger and the object and between the object and the environment.

1.1. Related works

1.1.1. Pushing. Planar sliding by means of pushing from a side of an object is a classic topic in robotics (Mason, 1982;

¹Istituto Italiano di Tecnologia (IIT), Italy

²Department of Information Engineering, University of Siena, Italy

Corresponding author:

M. Mahdi Ghazaei Ardakani, Istituto Italiano di Tecnologia (IIT), Department of Advanced Robotics (ADVR), Via Morego 30, 16163 Genoa, Italy.
Email: mahdi.ghazaei@control.lth.se

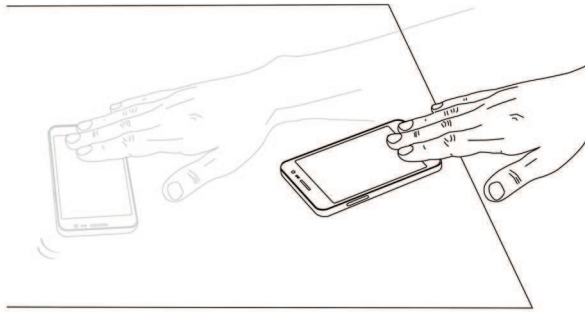


Fig. 1. An example in which the friction is utilized to move and reorient the cell phone.

Peshkin and Sanderson, 1987). Active sensing and pushing using only tactile feedback was proposed by Lynch et al. (1992). Ruiz-Ugalde et al. (2011) studied pushing objects with rectangular support. Under uncertainty of the center of pressure (COP), Huang et al. (2017) provided exact bounds for the motion of a sliding object. Pushing on the edge of blocks was revisited based on differential flatness for planning and control (Zhou and Mason, 2017). In these scenarios, the contact surface between the pusher and the object has been assumed small such that no moment can be transferred through the contact area. The studied problem in this article shares some of the properties of pushing. However, it differs in the fact that the relative motion of the pusher and the object is not rigidly restricted in any direction on the plane of motion, and the transfer of moment through the contact can be substantial. A major part of this article is devoted to deriving the properties of planar sliding using friction patches, which are the counterpart of the well-known properties of pushing. For this, we extend the notion of *motion cones* and *stable pushing*.

1.1.2. Pivoting. For the task of dynamic pivoting, assuming a “pivoting joint” and using a simple friction model, a robust controller was proposed to cope with the uncertainty in the torsional friction (Hou et al., 2016). In addition, adaptive control strategies have been considered by Viña B et al. (2016). Common simplifying assumptions used also in these works are that the contact points of the fingers and the object are fixed and/or the friction is isotropic with LSs described by diagonal matrices. In this work, we have relaxed these assumptions. However, in the appendix, we describe an approximate solution based on enforcing a pivoting joint to make the connection between this type of models and ours clear.

1.1.3. In-hand manipulation. In contrast to simple pivoting, friction patches have been considered for more complex in-hand manipulation tasks. Exploiting extrinsic dexterity, a grasped object can be manipulated. For example, Chavan-Dafle et al. (2018); Chavan-Dafle and Rodriguez (2017) have considered scenarios where objects

were pushed against various fixtures, while they were ensured to stick to the fixtures. A discrete set of hard point contacts was used to model the friction between the fixture and the object, while for the grasp the LS concept was utilized. These works can be regarded as an extension of pushing, in which the pusher establishes a large contact area. This makes the transfer of moment possible, but the relative motion is still rigidly constrained in the direction of interest.

Shi et al. (2017) derived a model of the sliding dynamics based on the LS contact model at each fingertip. The model is integrated forward to predict the motion of the object. By alternating between sticking and slipping phases, the planner finds a trajectory for regrasping. A quasi-static model can be considered as a special case of this model when the accelerating forces are small. However, we provide an explicit solution for the velocities under the quasi-static assumption. Our main contribution is an in-depth analysis of this solution. For example, three modes (sticking, pivoting, and slipping) are identified and the conditions for switching between them are specified. For planar sliding, the treatment of the *pivoting* mode, which happens when the soft finger slides against the object but can still impart movement on the latter, plays a crucial role. Moreover, the effect of varying the normal force is also taken into account in this article.

1.1.4. Generic framework. A generic manipulation problem with compliance and sliding was studied by Kao and Cutkosky (1992). In the subsequent articles, Kao and Cutkosky (1993); Xue and Kao (1994) analyzed manipulation of a business card on a frictionless table top using symmetric motion of two soft fingers. A good match between the theory and the experiments was reported. In these works, no explicit equation for the time evolution of the system is provided, which is required for certain applications and analysis. We derive a hybrid dynamical system, which allows to predict the modes of the system as well as the trajectory in time.

1.2. Problem formulation

This article presents a model for sliding an object on a planar surface with moment transfer using a soft finger. Consider the configuration shown in Figure 2. We refer to the part moving the object as a hand, which can be any part of a robotic hand such as a soft finger or in general a part of an end-effector. We assume that the object is rigid and the hand does not roll against it. The patch, which is the part of the hand in touch with the object, may however deform. Accordingly, we assign body-fixed frames to the object and to the patch. The frame \mathcal{H} is attached to the patch and the frame \mathcal{O} to the object. For convenience, we consider the frame of the object to be fixed at its center of mass (COM) with its z -axis orthogonal to the sliding surface. For the hand, we consider the frame to be fixed at the

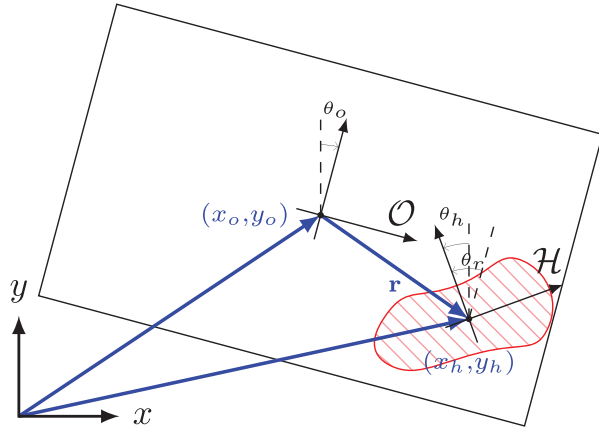


Fig. 2. The coordinate frames attached to the object \mathcal{O} and the patch \mathcal{H} .

centroid of the patch. Moreover, we assume that the (LSs) are symmetric with respect to the origin (if the direction of motion is reversed, so are friction forces). They can also be approximated by ellipsoids with respect to the COP.

The generalized coordinates of the object are denoted by

$$\mathbf{q}_o = [x_o, y_o, \theta_o]^T$$

and the twist and the wrenches expressed in the body-fixed frame are

$$\begin{aligned} \mathbf{v}_o &= [v_{xo}, v_{yo}, \omega_o]^T \\ \mathbf{w}_o &= [f_{xo}, f_{yo}, m_o]^T \end{aligned}$$

Similarly, the respective quantities for the friction patch are defined and denoted by the subscript h . We develop and analyze a model that can predict the motion of the object and the forces that are exchanged given \mathbf{v}_h .

Here is the list of the assumptions.

- The surface and the object are much more rigid compared with the robotic hand.
- The hand is placed on top of a flat object.
- The hand does not roll against the object.
- The Coulomb friction model is used.
- The velocity field of the patch can reasonably be approximated by a rigid motion.
- The LSs are symmetric with respect to the origin and can be approximated by ellipsoids.
- The inertial terms are small enough such that the quasi-static condition holds.

1.3. Abbreviations and nomenclature

Capital bold letters denote matrices, while small bold letters represent coordinate vectors. Scalars are typeset in roman.

LS	Limit surface
COM	Center of mass

COP	Center of pressure
COR	Center of rotation
HO	Hand-object
OE	Object-environment
\mathbf{q}_o	Generalized coordinates of the object
\mathbf{q}_h	Generalized coordinates of the patch
\mathbf{q}_{rel}	Relative coordinates of frame \mathcal{H} with respect to \mathcal{O}
\mathbf{v}_o	Twist of object with respect to frame \mathcal{O}
\mathbf{v}_h	Twist of patch with respect to frame \mathcal{H}
\mathbf{v}_h	Linear velocity of the patch
\mathbf{v}_{rel}	Relative twist of patch and object in \mathcal{H}
\mathbf{w}_o	Wrenches exerted on the object by the environment in \mathcal{O}
\mathbf{w}_h	Wrenches exerted on the hand through the patch in \mathcal{H}
\mathbf{p}	Position of the pivot point with respect to frame \mathcal{H}
\mathbf{m}	Torque
$\mathbf{J}(\mathbf{r})$	Jacobian for a point at relative coordinates \mathbf{r}
$\mathbf{R}(\theta)$	Rotation matrix along the z direction with θ rad
$\mathbf{G}(\mathbf{q})$	Jacobian for a frame with relative coordinates \mathbf{q}
\mathbf{A}	LS of OE contact with respect to frame \mathcal{O}
\mathbf{B}	LS of HO contact with respect to frame \mathcal{H}
$\hat{\mathbf{A}}$	LS of OE contact with respect to frame \mathcal{H}
Φ	Principal sliding wrenches
Λ	Generalized eigenvalues of $\hat{\mathbf{A}}$ and \mathbf{B}

1.4. Outline

Section 2 summarizes the background information for coordinate transformations and the friction model. In Section 3, the formulation of a hybrid dynamical system is derived, which can determine the active mode (*slipping*, *sticking*, or *pivoting*), and predict the motion and force trajectories.

A number of interesting properties of this system are explored in Section 4, for instance the conditions and boundaries where the system is stable, which can be useful when using this model for planning and control.

In Section 5, the experimental evaluation of the model is explained as well as a practical application, where an object is steered along a defined trajectory through the control of the finger normal force. Finally, a discussion of the findings and the conclusions of this article are presented in Sections 6 and 7, respectively.

2. Preliminaries

The relative coordinates of frame \mathcal{H} with respect to \mathcal{O} can be written as

$$\begin{aligned} \mathbf{q}_{\text{rel}} &:= [x_r, y_r, \theta_r]^T \\ &= \mathbf{R}(-\theta_o)(\mathbf{q}_h - \mathbf{q}_o) \end{aligned}$$

where $\mathbf{R}(\cdot)$ is the rotation matrix along the z -axis

$$\mathbf{R}(\theta) := \begin{bmatrix} \cos(\theta) & -\sin(\theta) & 0 \\ \sin(\theta) & \cos(\theta) & 0 \\ 0 & 0 & 1 \end{bmatrix} \quad (1)$$

We also define for a position vector $\mathbf{r} = [x_r, y_r]^T$,

$$\mathbf{J}(\mathbf{r}) := \begin{bmatrix} 1 & 0 & -y_r \\ 0 & 1 & x_r \\ 0 & 0 & 1 \end{bmatrix} \quad (2)$$

with the property that $\mathbf{J}(\mathbf{r}_1)\mathbf{J}(\mathbf{r}_2) = \mathbf{J}(\mathbf{r}_1 + \mathbf{r}_2)$ for any \mathbf{r}_1 and \mathbf{r}_2 . Accordingly,

$$\mathbf{J}^{-1}(\mathbf{r}) = \mathbf{J}(-\mathbf{r}) = \begin{bmatrix} 1 & 0 & y_r \\ 0 & 1 & -x_r \\ 0 & 0 & 1 \end{bmatrix}$$

The relation between planar twists \mathbf{v}_p given in frame \mathcal{P} and \mathbf{v}_o given in frame \mathcal{O} is (Featherstone, 2008)

$$\mathbf{v}_p = \mathbf{G}\mathbf{v}_o \quad (3)$$

where

$$\mathbf{G} := \mathbf{G}(\mathbf{q}_{\text{rel}}) = \mathbf{R}^T(\theta_r) \mathbf{J}(\mathbf{r}) \quad (4)$$

Similarly, the wrenches are related according to

$$\mathbf{w}_o = \mathbf{G}^T \mathbf{w}_p \quad (5)$$

The friction wrench with respect to point o , under the assumption of the Coulomb friction between surfaces, can be calculated as (Mason, 1982)

$$\mathbf{f}_o = - \int_D \frac{\mathbf{v}(\mathbf{r})}{\|\mathbf{v}(\mathbf{r})\|} \mu_r p(\mathbf{r}) \, dA \quad (6a)$$

$$\mathbf{m}_o = - \int_D \frac{(\mathbf{r} - \mathbf{o}) \times \mathbf{v}(\mathbf{r})}{\|\mathbf{v}(\mathbf{r})\|} \mu_r p(\mathbf{r}) \, dA \quad (6b)$$

where $p(\mathbf{r})$ denotes the pressure and $\mathbf{v}(\mathbf{r})$ denotes the relative linear velocity between sliding surfaces at position \mathbf{r} . The integral is calculated over the area D . Based on our assumptions, the relation between (6a) and (6b) can be approximated by an implicit function

$$H(\mathbf{w}) := \mathbf{w}^T \mathbf{A} \mathbf{w} = 1 \quad (7)$$

for a symmetric positive-definite matrix $\mathbf{A} \in \mathbb{R}^{3 \times 3}$. This defines a generic quadratic form which subsumes the ellipsoid approximation of the LS suggested by Howe and Cutkosky (1996). The corresponding twist is parallel to the gradient of $H(\mathbf{w})$. Thus,

$$\begin{aligned} \mathbf{v} &= -k' \nabla H(\mathbf{w}) \\ &= -k \mathbf{A} \mathbf{w}, \quad k \geq 0 \end{aligned} \quad (8)$$

where k is a proportionality constant. Note that for a given \mathbf{w} applied to an object sliding on a surface, there will be no relative motion if

$$H(\mathbf{w}) < 1$$

and the object will be accelerating if $H(\mathbf{w})$ is larger than one. By combining (7) and (8), it is possible to eliminate k and, hence, to find wrenches as a function of the twist

$$\mathbf{w} = - \frac{\mathbf{A}^{-1} \mathbf{v}}{\sqrt{\mathbf{v}^T \mathbf{A}^{-1} \mathbf{v}}} \quad (9)$$

Proposition 1. Assume that the LS calculated with respect to frame \mathcal{O} can be represented by

$$\mathbf{w}_o^T \mathbf{A} \mathbf{w}_o = 1 \quad (10)$$

where \mathbf{A} is a positive-definite matrix. Then, the LS with respect to frame \mathcal{P} , which has the relative coordinates $[\mathbf{r}, \theta_r]^T$, is

$$\mathbf{w}_p^T \hat{\mathbf{A}} \mathbf{w}_p = 1 \quad (11)$$

$$\hat{\mathbf{A}} = \mathbf{G} \mathbf{A} \mathbf{G}^T \quad (12)$$

is a positive-definite matrix and $\mathbf{G} = \mathbf{R}^T(\theta_r) \mathbf{J}(\mathbf{r})$.

Proof. The result is achieved by the direct application of (5). For the positive-definiteness, note that

$$\mathbf{w}^T \hat{\mathbf{A}} \mathbf{w} = (\mathbf{G}^T \mathbf{w})^T \mathbf{A} (\mathbf{G}^T \mathbf{w}) \geq 0$$

Since \mathbf{G} is full rank, $\mathbf{G}^T \mathbf{w}$ is zero if and only if $\mathbf{w} = \mathbf{0}$. Consequently, the matrix $\hat{\mathbf{A}}$ is positive-definite. ■

The following theorem shows that a LS, which is characterized by any symmetric positive-definite matrix, can be assumed as a diagonal matrix with respect to a frame assigned at the COP.

Theorem 2. Any symmetric matrix $\mathbf{A} \in \mathbb{R}^{3 \times 3}$ can be decomposed as

$$\mathbf{A} = \mathbf{R}^T \mathbf{J} \mathbf{A} \mathbf{J}^T \mathbf{R} \quad (13)$$

where \mathbf{A} is a diagonal matrix, and \mathbf{R} and \mathbf{J} are rotation and Jacobian matrices as defined in (1) and (2), respectively.

Proof. See Appendix B. ■

As a consequence of Theorem 2, the matrix describing the LS is diagonal in a proper coordinate frame. Accordingly, the typical assumption about the structure of the matrix can be removed. This property is also useful for the identification of the LS and COP.

3. Model for planar sliding

3.1. Governing equations

The LSs and the relation between the friction wrench exerted on the hand through the patch, \mathbf{w}_h , and the wrench affecting the object through the underlying surface, \mathbf{w}_o are

$$\mathbf{w}_o^T \mathbf{A} \mathbf{w}_o = 1 \quad (14)$$

$$\mathbf{w}_h^T \mathbf{B} \mathbf{w}_h = 1 \quad (15)$$

$$\mathbf{w}_o - \mathbf{G}^T \mathbf{w}_h = \mathbf{0} \quad (16)$$

where $\mathbf{G} := \mathbf{G}(\mathbf{q}_{\text{rel}})$ denotes the Jacobian corresponding to the relative coordinates of frame \mathcal{H} with respect to \mathcal{O} . Equation (16) is derived from the fact that the wrenches

on the object sum to zero under the assumption of quasi-static manipulation, i.e., the inertial forces are negligible. In addition, we have the velocity relations

$$\mathbf{v}_o = -k_1 \mathbf{A} \mathbf{w}_o, \quad k_1 \geq 0 \quad (17)$$

$$\mathbf{v}_{\text{rel}} = -k_2 \mathbf{B} \mathbf{w}_h, \quad k_2 \geq 0 \quad (18)$$

$$\mathbf{v}_{\text{rel}} = \mathbf{v}_h - \mathbf{G} \mathbf{v}_o \quad (19)$$

where \mathbf{v}_{rel} denotes the relative twist of the patch with respect to the object expressed in \mathcal{H} . Equations (17) and (18) are the counterparts of (8) whereas (19) is obtained by first transforming \mathbf{v}_o to the frame of the patch and then subtracting it from the twist of the patch.

3.2. Solution

Using (16) it is possible to rewrite (14) as

$$\mathbf{w}_h^T \hat{\mathbf{A}} \mathbf{w}_h = 1 \quad (20)$$

where $\hat{\mathbf{A}} = \mathbf{G} \mathbf{A} \mathbf{G}^T$ characterizes the LS of the object at frame \mathcal{H} . By solving the generalized eigenvalue problem $\mathbf{B} \Phi = \hat{\mathbf{A}} \Phi \Lambda$, we can simultaneously diagonalize $\hat{\mathbf{A}}$ and \mathbf{B} such that

$$\Lambda = \Phi^T \mathbf{B} \Phi$$

$$\mathbf{I} = \Phi^T \hat{\mathbf{A}} \Phi$$

where $\mathbf{I} \in \mathbb{R}^{3 \times 3}$ denotes the identity matrix. Thus, by applying $\mathbf{w}_h = \Phi \mathbf{w}$ we transform (15) and (20) to

$$\mathbf{w}^T \Lambda \mathbf{w} = 1 \quad (21a)$$

$$\mathbf{w}^T \mathbf{w} = 1 \quad (21b)$$

Moreover, by subtracting (21b) from (21a), we find the normal form

$$\mathbf{w}^T \mathbf{C} \mathbf{w} = 0 \quad (22a)$$

$$\mathbf{w}^T \mathbf{w} = 1 \quad (22b)$$

where $\mathbf{C} := \Lambda - \mathbf{I}$ is a diagonal matrix. Note that if there is a solution to (22), it is possible to recover the wrenches at the patch and the object frames using the following relations

$$\mathbf{w}_h = \Phi \mathbf{w} \quad (23a)$$

$$\mathbf{w}_o = \mathbf{G}^T \mathbf{w}_h \quad (23b)$$

In view of (21), the transformed LSs can be represented by a unit sphere and an ellipsoid, as shown in Figure 3. Accordingly, there are several possible cases.

- The LS of the object lies entirely inside the LS of the patch, hence $\mathbf{C} < 0$. Since any required forces for sliding can be provided through the patch, the hand sticks to the object ($\mathbf{v}_{\text{rel}} = \mathbf{0}$). The only possible mode in this case is called *sticking*.

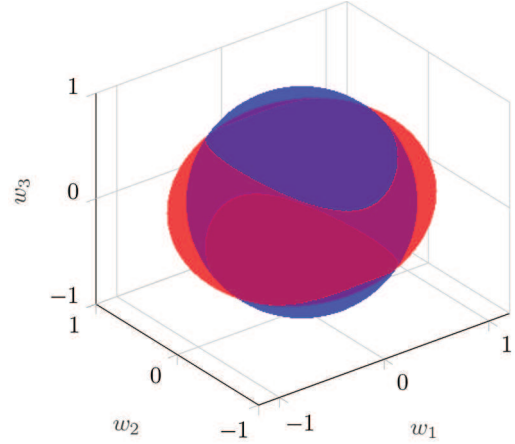


Fig. 3. Visualization of (21), i.e., transformed LSs for the patch (red ellipsoid $\mathbf{w}^T \Lambda \mathbf{w} = 1$) and for the object (the unit sphere $\mathbf{w}^T \mathbf{w} = 1$ in blue). In this example, pivoting mode is possible since the surfaces intersect. The vector \mathbf{w} is unitless.

- The LS of the patch is entirely contained in the LS of the object, hence $\mathbf{C} > 0$. In this case, the hand cannot provide enough force through the patch for sliding the object against the surface, hence the object remains still and the patch slides against it ($\mathbf{v}_o = \mathbf{0}$). We call the corresponding mode *slipping*.
- Otherwise, there exists a solution to (21) and the hand can move the object while allowing it to slide. We call this mode *pivoting*. An example in which this mode is possible is illustrated in Figure 3, and arises when the hand applies a wrench that lies on the intersection of the red ellipsoid and the blue sphere. Other modes are also possible in this situation, such as the hand slipping against the object (points on the red ellipsoid surface and inside the blue sphere), and sticking to it (points inside the red ellipsoid and outside the blue sphere).

Using the transformations (23), it is also possible to rewrite (17)–(19) to obtain

$$\Phi^T \mathbf{G} \mathbf{v}_o = -k_1 \mathbf{w}, \quad k_1 \geq 0 \quad (24)$$

$$\Phi^T \mathbf{v}_{\text{rel}} = -k_2 \Lambda \mathbf{w}, \quad k_2 \geq 0 \quad (25)$$

$$\mathbf{v}_{\text{rel}} = \mathbf{v}_h - \mathbf{G} \mathbf{v}_o \quad (26)$$

From (24)–(26), we conclude

$$\tilde{\mathbf{v}}_h = -(k_1 \mathbf{I} + k_2 \Lambda) \mathbf{w}$$

where $\tilde{\mathbf{v}}_h := \Phi^T \mathbf{v}_h$. Let us define $\alpha = \frac{k_2}{k_1} \geq 0$. Accordingly,

$$\mathbf{w} = -\frac{1}{k_1} (\mathbf{I} + \alpha \Lambda)^{-1} \tilde{\mathbf{v}}_h \quad (27)$$

Substituting (27) into (22a) results in

$$\tilde{\mathbf{v}}_h^T \mathbf{C} (\mathbf{I} + \alpha \Lambda)^{-2} \tilde{\mathbf{v}}_h = 0 \quad (28)$$

which is equivalent to

$$c_1 \left(\frac{\tilde{v}_{xh}}{\alpha\lambda_1 + 1} \right)^2 + c_2 \left(\frac{\tilde{v}_{yh}}{\alpha\lambda_2 + 1} \right)^2 + c_3 \left(\frac{\tilde{\omega}_h}{\alpha\lambda_3 + 1} \right)^2 = 0 \quad (29)$$

where c_i and λ_i are the diagonal elements of \mathbf{C} and $\mathbf{\Lambda}$, respectively. Equation (29) can be solved for α . Afterwards, by substituting (27) into (22b), it is possible to calculate k_1 .

A relation between \mathbf{v}_o and \mathbf{v}_h can also be found by substituting (27) back to (24)

$${}_h\tilde{\mathbf{v}}_o = (\mathbf{I} + \alpha\mathbf{\Lambda})^{-1} \tilde{\mathbf{v}}_h$$

After some algebraic manipulations, we have

$$\begin{aligned} {}_h\mathbf{v}_o &= \hat{\mathbf{A}}(\hat{\mathbf{A}} + \alpha\mathbf{B})^{-1} \mathbf{v}_h \\ &= (\mathbf{I} + \alpha\mathbf{B}\hat{\mathbf{A}}^{-1})^{-1} \mathbf{v}_h \end{aligned} \quad (30)$$

where ${}_h\mathbf{v}_o := \mathbf{G}\mathbf{v}_o$ is the twist of the object expressed in \mathcal{H} . Using (26), we find the relative twist to be

$$\begin{aligned} \mathbf{v}_{\text{rel}} &= (\mathbf{I} + (\alpha\mathbf{B}\hat{\mathbf{A}}^{-1})^{-1})^{-1} \mathbf{v}_h \\ &= \alpha(\alpha\mathbf{I} + \hat{\mathbf{A}}\mathbf{B}^{-1})^{-1} \mathbf{v}_h \end{aligned} \quad (31)$$

When the patch slides against the object, there is a pivot point, which can be determined by finding the point where the object and the patch have the same velocity. In other words, the *pivot point* is the instantaneous center of rotation (COR) between the patch and the object. Using the velocity transfer relation according to (3), we conclude the location of the pivot point in the hand frame is

$$\mathbf{p} := [x_p, y_p]^T = \frac{1}{\omega_r} [-v_{yr}, v_{xr}]^T \quad (32)$$

where $\mathbf{v}_{\text{rel}} = [v_{xr}, v_{yr}, \omega_r]^T$ denotes the relative twist of the patch with respect to the object expressed in \mathcal{H} .

In sticking mode, the pivot point is indeterminate and we may choose any point, e.g., the origin of \mathcal{H} . However, at the boundary of pivoting and sticking modes, it is possible to make the pivot point a continuous function by evaluating the limit as $\alpha \rightarrow 0$. In view of (31), this is equivalent of substituting \mathbf{v}_{rel} in (32) with

$$\tilde{\mathbf{v}}_{\text{rel}} = \mathbf{B}\hat{\mathbf{A}}^{-1} \mathbf{v}_h$$

It is also possible to develop an approximate solution to the problem of determining the velocity of the object in pivoting mode assuming that the displacement of the pivot point is limited, e.g., when the torsional friction of the patch is small. This result is of interest for understanding the relation of the presented model to “pivoting joint” and pulling/pushing models. This approach is detailed in Appendix A.

3.3. Regions of validity

If there is $\alpha > 0$ to satisfy (29), the pivoting mode is active, which implies having a finite pivot point. Otherwise,

the wrenches can be calculated to identify which mode is valid. In sticking mode, from the twist of the patch and the fact that the object slides on the surface, we can easily calculate \mathbf{w}

$$\tilde{\mathbf{v}}_h = -k_1 \mathbf{w} \quad (33a)$$

$$1 = \mathbf{w}^T \mathbf{w} \quad (33b)$$

Then, the sticking mode is valid if the contact between the patch and the object can be sustained by the friction, i.e.,

$$\mathbf{w}^T \mathbf{\Lambda} \mathbf{w} < 1 \quad (34)$$

Subtracting (33b) from (34) results in

$$\mathbf{w}^T \mathbf{C} \mathbf{w} < 0 \quad (35)$$

Using (33a), it is possible rewrite the condition as

$$\tilde{\mathbf{v}}_h^T \mathbf{C} \tilde{\mathbf{v}}_h < 0 \quad (36)$$

Note that whenever $\alpha = 0$, the relative velocity is zero and, hence, the mode is sticking. Since in this case Equation (28) degenerates to condition (36) with an equality sign, we extend the condition to include also its boundary. Accordingly, in sticking mode

$$\tilde{\mathbf{v}}_h^T \mathbf{C} \tilde{\mathbf{v}}_h \leq 0 \quad (37)$$

or, equivalently,

$$\mathbf{v}_h^T \hat{\mathbf{A}}^{-1} (\mathbf{B} - \hat{\mathbf{A}}) \hat{\mathbf{A}}^{-1} \mathbf{v}_h \leq 0 \quad (38)$$

Similarly, in slipping mode

$$\tilde{\mathbf{v}}_h = -k_2 \mathbf{\Lambda} \mathbf{w} \quad (39a)$$

$$1 = \mathbf{w}^T \mathbf{\Lambda} \mathbf{w} \quad (39b)$$

and the mode is valid if

$$\mathbf{w}^T \mathbf{w} < 1 \quad (40)$$

Subtracting (40) from (39b) results in

$$\mathbf{w}^T \mathbf{C} \mathbf{w} > 0$$

Using a similar argument as mentioned previously, we extend the boundary to include the case $\alpha \rightarrow \infty$ and express the condition using (39a) as

$$\tilde{\mathbf{v}}_h^T \mathbf{C} \mathbf{\Lambda}^{-2} \tilde{\mathbf{v}}_h = \tilde{\mathbf{v}}_h^T \mathbf{C} (\mathbf{C} + \mathbf{I})^{-2} \tilde{\mathbf{v}}_h \geq 0 \quad (41)$$

or, equivalently,

$$\mathbf{v}_h^T \mathbf{B}^{-1} (\hat{\mathbf{A}} - \mathbf{B}) \mathbf{B}^{-1} \mathbf{v}_h \geq 0 \quad (42)$$

3.4. Dynamical system

The quasi-static behavior of the system is determined based on the modes of the system. There are three modes depending on which contact surface can provide enough friction to avoid slippage. To determine the active mode, i.e., the discrete state of the system, when $\mathbf{v}_h \neq 0$ first we solve (29). If there is a positive real solution, then the pivoting mode is selected. Otherwise, depending on whether the condition (37) or (41) is fulfilled, sticking or slipping mode is selected, respectively. When $\mathbf{v}_h = 0$, the definition of the mode is somewhat arbitrary. Hence, if neither $\mathbf{C} < 0$ nor $\mathbf{C} > 0$, we set the mode to pivoting. This procedure is summarized in Algorithm 1.

By integrating the twists in the global frame, we find the generalized coordinates of the patch and the object. This implies the dynamical system

$$\dot{\mathbf{q}}_h = \mathbf{R}(\theta_h) \mathbf{v}_h \quad (43a)$$

$$\dot{\mathbf{q}}_o = \mathbf{R}(\theta_o) \mathbf{v}_o \quad (43b)$$

In pivoting mode, i.e., when $\exists \alpha > 0$, using (30) we find

$$\mathbf{v}_o = \mathbf{G}^{-1} \left(\mathbf{I} + \alpha \mathbf{B} \hat{\mathbf{A}}^{-1} \right)^{-1} \mathbf{v}_h \quad (44)$$

where $\mathbf{G} := \mathbf{G}(\mathbf{q}_{\text{rel}})$ and $\mathbf{q}_{\text{rel}} = \mathbf{R}(-\theta_o)(\mathbf{q}_h - \mathbf{q}_o)$. Otherwise, in sticking mode, using (26) and the fact that $\mathbf{v}_{\text{rel}} = 0$ we obtain

$$\mathbf{v}_o = \mathbf{G}^{-1} \mathbf{v}_h \quad (45)$$

In slipping mode, the velocity of the object is zero,

$$\mathbf{v}_o = \mathbf{0} \quad (46)$$

The wrenches at the hand \mathbf{w}_h can also be expressed in terms of the states and \mathbf{v}_o , which in turn is a function of the input. Using (9) together with (16), we conclude

$$\mathbf{w}_h = -\frac{\mathbf{G}^{-T} \mathbf{A}^{-1} \mathbf{v}_o}{\sqrt{\mathbf{v}_o^T \mathbf{A}^{-1} \mathbf{v}_o}} \quad (47)$$

Accordingly, in pivoting mode using (44) we have

$$\mathbf{w}_h = -\frac{1}{k_1} \left(\hat{\mathbf{A}} + \alpha \mathbf{B} \right)^{-1} \mathbf{v}_h \quad (48)$$

where

$$k_1 = \left(\mathbf{v}_h^T \left(\hat{\mathbf{A}} + \alpha \mathbf{B} \right)^{-1} \hat{\mathbf{A}} \left(\hat{\mathbf{A}} + \alpha \mathbf{B} \right)^{-1} \mathbf{v}_h \right)^{1/2}$$

and in sticking mode,

$$\mathbf{w}_h = -\frac{\hat{\mathbf{A}}^{-1} \mathbf{v}_h}{\sqrt{\mathbf{v}_h^T \hat{\mathbf{A}}^{-1} \mathbf{v}_h}} \quad (49)$$

In slipping mode, $\mathbf{v}_r = \mathbf{v}_h$. Therefore, using (9) it is concluded that

$$\mathbf{w}_h = -\frac{\mathbf{B}^{-1} \mathbf{v}_h}{\sqrt{\mathbf{v}_h^T \mathbf{B}^{-1} \mathbf{v}_h}} \quad (50)$$

3.5. Effect of normal forces

Our formulation is generic with respect to \mathbf{A} and \mathbf{B} describing the LSSs, as long as the matrices are positive-definite. In fact, both matrices can be time-varying, specifically when the COP of the object does not have a fixed transformation to its COM or when the patch is deforming as a result of variations in normal or tangential forces.

For surfaces with homogeneous friction coefficients and symmetrical pressure distributions, with no deformation of contact areas as a result of varying normal forces, the trajectory depends only on the ratio between normal forces at the hand-object (HO) and the object-environment (OE) contacts, and not their absolute values. The reason is that given these assumptions, the normal forces as well as the friction coefficients can be factorized from \mathbf{A} and \mathbf{B} , and in the solution only the ratio will appear. Nevertheless, the friction forces will be scaled.

In general, when the normal force at the patch is changed, the frictions related to HO and OE are not proportionally changed. First, the lower surface has to additionally support the weight of the object; second, the pressure distribution may vary and become stronger closer to the patch; and, third, deformation of the patch may increase its contact area.

To exactly model the effect of normal force, it is required to know the pressure distributions and their variation. This is not a simple task as the pressure distribution depends in general on the stiffness of the contact surfaces, geometry of the contact, and relative velocities. In particular, the friction patch may go through large deformations as a function of normal forces.

To get an understanding of the effect of normal force, consider a special case where a flat object and a sphere-shaped soft finger following a Hertzian law are in contact. Denoting the normal force on the sphere by f_n , the pressure distribution at radius r is (Johnson, 1985)

$$p(r) = p_0 \left(1 - \frac{r^2}{a^2} \right)^{1/2} \quad (51)$$

where

$$p_0 = \frac{3}{2\pi a^2} f_n \quad (52)$$

and a is the radius of the contact area. Using this pressure distribution, Equation (6) allows us to calculate the maximum friction force and torque

$$f_{\text{max}} = \mu f_n \quad (53)$$

$$m_{\text{max}} = \mu \frac{3\pi}{16} a f_n \quad (54)$$

By changing the normal force, the radius of the contact area increases according to

$$a = \left(\frac{3}{4} \frac{R}{E^*} f_n \right)^{1/3} \quad (55)$$

Algorithm 1. Mode selection.

$\mathbf{v}_h \neq 0$	$\mathbf{v}_h = 0$
1: Solve for α in (29)	1: if $\mathbf{C} < 0$ then
2: if $\exists \alpha > 0$ then	2: mode \leftarrow sticking
3: mode \leftarrow pivoting	3: else if $\mathbf{C} > 0$ then
4: else if $\tilde{\mathbf{v}}_h^T \mathbf{C} \tilde{\mathbf{v}}_h \leq 0$ then	4: mode \leftarrow slipping
5: mode \leftarrow sticking	5: else
6: else	6: mode \leftarrow pivoting
7: mode \leftarrow slipping	7: end if
8: end if	

where R is the radius of the sphere and E^* is the effective elastic modulus. As can be seen, while tangential forces depend linearly on the normal force, the torque has a non-linear dependence because of the increase in the contact area. Accordingly, it is possible to change the ratio of the torsional to tangential friction of the patch.

Another observation is that by pressing the patch harder, the COP of the object shifts more toward the patch. Although modeling the exact physical phenomenon is complicated, we can easily incorporate this effect using a computational model. For example, define $s \in \mathbb{R}$ to be a value between zero and one characterizing the percentage of the shift of the COP

$$s = 1 - \left(c \frac{f_n}{mg} + 1 \right)^{-\delta} \quad (56)$$

where c and δ are model parameters and mg is the weight of the object. Then, if the LS at the COP of the object is characterized by \mathbf{A}_{COP} and \mathbf{r} denotes the relative position of the hand frame with respect to the object frame, the LS at the object frame is

$$\mathbf{A} = \mathbf{J}(-s\mathbf{r}) \mathbf{A}_{\text{COP}} \mathbf{J}^T(-s\mathbf{r}) \quad (57)$$

A similar approach can be used to compensate for the shift of COPs due to relative velocities. See Appendix E for experimental validation of the proposed model for the shift of COP.

4. Properties of sliding motion

In this section, we describe a number of properties of the quasi-static sliding motion. Some are general properties concerning the well-posedness of the problem and some are useful results for planning and control.

4.1. Well-posedness of the problem

If none of the diagonal elements of \mathbf{C} is zero, i.e., the matrix is full rank, we can prove that there is always a unique solution to the system. First, we prove that there could exist at most one solution in pivoting mode. Second, we prove that there exists at least one active mode and it is impossible to have any two modes active at the same time. Note that when \mathbf{C} is rank deficient, \mathbf{v}_o is indeterminate for certain \mathbf{v}_h

since the forces can be balanced for any value of $\alpha \geq 0$. For example, in one-dimensional space, as a consequence of Coulomb friction model, if the friction force at HO contact is exactly the same as the friction at OE contact, the object can have any velocity in the range from zero to the hand velocity.

Theorem 3. *If \mathbf{C} is full rank and $\mathbf{v}_h \neq 0$, there is at most one positive solution ($\alpha > 0$) to Equation (29).*

Proof. See Appendix C. ■

Theorem 4. *If \mathbf{C} is full rank and $\mathbf{v}_h \neq 0$, the mode is uniquely determined.*

Proof. See Appendix D. ■

Note that the transition between modes can happen smoothly. For example, the pivot point can gradually shift to infinity as the patch starts to slide against the object or go to a limit value as the patch and the object approach the same velocity.

4.2. Invariance

Theorem 5. *Scaling the twist of the patch by a constant results in the twist of the object being scaled by the same constant, i.e., if \mathbf{v}_h results in \mathbf{v}_o , then $c\mathbf{v}_h$ results in $c\mathbf{v}_o$.*

Proof. Note that α which is the solution to (29) is not affected by scaling \mathbf{v}_h . The proof is completed by considering the relations (44) and (45). ■

Corollary 1. *Reversing the twist of the patch reverses the twist of the object, which is proved by setting $c = -1$.*

Corollary 2. *When $\omega_h = 0$, the location of the pivot point as a function of the velocity direction is periodic with period π . The proof is straightforward by considering (31) and (32).*

Note that Corollary 1 does not guarantee that reversing a trajectory will bring the object back to its initial state. This is due to the sensitivity of the dynamical system to perturbations, e.g., reversing from the vicinity of a fixed point is very sensitive to noise.

Theorem 6. *Given the quasi-static assumption for sliding, the path of the object is invariant under scaling of the patch twist according to $c\mathbf{v}_h(ct)$ for any constant $c \in \mathbb{R} \neq 0$.*

Proof. Let us define $\tilde{\mathbf{q}}_o(t) := \mathbf{q}_o(ct)$ where $\mathbf{q}_o(t)$ is the solution of (43b). Accordingly, we conclude

$$\dot{\tilde{\mathbf{q}}}_o = \mathbf{R}(\tilde{\theta}_o) c\mathbf{v}_o(ct) \quad (58)$$

From Theorem 5, it is clear that $c\mathbf{v}_h(ct)$ results in $c\mathbf{v}_o(ct)$. Thus, $\tilde{\mathbf{q}}_o(t)$ is the solution of the system with the scaled input velocity. Since a path is independent of its parametrization, the path defined by $\mathbf{q}_o(t)$ is the same as $\tilde{\mathbf{q}}_o(t)$. ■

Corollary 3. *Starting from the same initial configuration and moving the patch along a line at a constant velocity, the distance required for the patch to move for causing a certain change in the orientation of the object, $\Delta\theta_o$, is independent of the velocity.*

This is a useful fact for planning, meaning that if the object that has to be reoriented is lying close to the edge of a surface, simply increasing the linear velocity cannot increase the amount of rotation before reaching the edge.

4.3. Motion cones

It is possible to characterize the set of patch twists corresponding to each mode of the system. As we will prove, these sets define cones in twist space. This allows us to define a similar concept to the *motion cones* that appeared in the work of Mason (1986) and Lynch and Mason (1996), defining the set of possible velocities for stable pushing, i.e., when the pusher does not slide against the object. In this article, we use the term more generically to refer to twist subspaces corresponding to any modes, i.e., we may use slipping, sticking, and pivoting motion cones. However, unless specified, by a motion cone we also mean the subspace corresponding to sticking mode.

Theorem 7. *The boundary of each mode in twist space of the patch is a conical surface. The set of patch motions for which the object sticks to the patch or slips against it defines a cone. Accordingly, the pivoting mode is the intersection of the complement of these two cones.*

Proof. The theorem is a direct consequence of the regions of validity in Section 3.3. According to (37), sticking mode is valid if

$$\tilde{\mathbf{v}}_h^T \mathbf{C} \tilde{\mathbf{v}}_h \leq 0 \quad (59)$$

and the boundary is obtained with the equality sign. Similarly, for slipping mode from (41) we have

$$\tilde{\mathbf{v}}_h^T \mathbf{C} (\mathbf{C} + \mathbf{I})^{-2} \tilde{\mathbf{v}}_h \geq 0 \quad (60)$$

These equations define closed cone sets in the form of the interior and the exterior of elliptic cones, depending on the

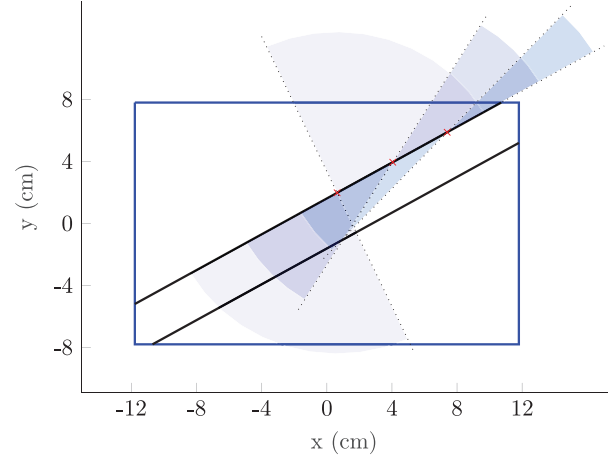


Fig. 4. An example of the result of Corollary 4. For three different hand positions (red cross), the sticking motion cones are shaded. That is, if the velocity vector \mathbf{v}_h drawn in \mathcal{H} frame lies inside any of these cones, the object sticks to the hand. The two black lines visualize the locus of all patch locations sharing the same boundary of the planar motion cone, $\mathbf{v}_h = [\sqrt{3}, 1]^T$.

signs of the diagonal elements of \mathbf{C} . The intersection of the complement of these sets defines the region of validity for pivoting motion, i.e.,

$$\left\{ \tilde{\mathbf{v}}_h : \tilde{\mathbf{v}}_h^T \mathbf{C} \tilde{\mathbf{v}}_h > 0 \wedge \tilde{\mathbf{v}}_h^T \mathbf{C} (\mathbf{C} + \mathbf{I})^{-2} \tilde{\mathbf{v}}_h < 0 \right\} \quad (61)$$

By changing the basis according to $\tilde{\mathbf{v}}_h = \Phi^T \mathbf{v}_h$, the proof is complete. ■

The following theorem allows us to define bounds for the direction of the patch velocity that leads to pivoting mode.

Theorem 8. *If $\omega_h = 0$, there is either no \mathbf{v}_h for pivoting mode, or \mathbf{v}_h lies inside a planar cone or two planar cones.*

Proof. According to Theorem 7, the region of pivoting mode in twist space is the intersection of two cone sets with vertices at the origin. Considering the intersection of this set with the plane $\omega_h = 0$, the proof is complete. ■

Since the motion cones depend on the position of a patch, we always draw them with respect to \mathcal{H} . Note that the motion cones are three-dimensional objects in twist space. In two-dimensional space, we draw the intersection of the cone with the ω_h plane and overlay it in the Cartesian space. When $\omega_h = 0$ the resulting intersection is a planar cone. However, when $\omega_h \neq 0$, the intersection can be any conic section. Unlike pushing results, this implies that changing the magnitude of the linear velocity may result in a mode change.

Theorem 9. *Assume variations of \mathbf{A} with respect to hand placements are negligible. Then, the locus of patch positions with the same \mathbf{v}_h characterizing the boundary of the planar motion cone ($\omega_h = 0$) is composed of at most two parallel lines.*

Proof. The boundary of the planar motion cone is characterized by $\mathbf{v}_h := [\mathbf{v}_h^T, 0]^T$ that solves (38) with the equality sign. Expanding the expression, we find

$$\mathbf{v}_h^T \hat{\mathbf{A}}^{-1} \mathbf{B} \hat{\mathbf{A}}^{-1} \mathbf{v}_h = \mathbf{v}_h^T \hat{\mathbf{A}}^{-1} \mathbf{v}_h \quad (62)$$

The Jacobian matrix $\mathbf{G}(\mathbf{q}_{\text{rel}})$ is a function of the relative position of the patch and the object, $\mathbf{r} = [x_r, y_r]$. As a result

$$\hat{\mathbf{A}}^{-1} = \mathbf{G}^{-T} \mathbf{A}^{-1} \mathbf{G}^{-1} \quad (63)$$

varies with the change of the patch position. Since ω_h is zero,

$$\mathbf{G}^{-1} \mathbf{v}_h = \mathbf{R} \mathbf{v}_h \quad (64)$$

Thus, the right-hand side of (62) is independent of \mathbf{r} . The left-hand side can be written as

$$\mathbf{u}^T \mathbf{J}^{-1} \mathbf{R} \mathbf{B} \mathbf{R}^T \mathbf{J}^{-T} \mathbf{u} \quad (65)$$

where $\mathbf{u} = \mathbf{A}^{-1} \mathbf{G}^{-1} \mathbf{v}_h$ is also independent of \mathbf{r} because of $\omega_h = 0$. Assuming $\mathbf{u} = [u_1, u_2, u_3]^T$, we find

$$\mathbf{u}^T \mathbf{J}(-\mathbf{r}) = [u_1, u_2, u_1 y_r - u_2 x_r + u_3] \quad (66)$$

Accordingly, Equation (62) defines a second-order equation in $u_1 y_r - u_2 x_r + u_3$. This completes the proof that if there are any solutions for $[x_r, y_r]$, they can form at most two lines with the slope $-u_2/u_1$. ■

Corollary 4. *If \mathbf{A} characterizes an isotropic friction, moving \mathcal{H} along one boundary of a motion cone keeps that boundary intact for the new patch position.*

Proof. In this case, $\mathbf{u} = [u_1, u_2, 0]^T$ and is aligned with the velocity of the patch in the object frame. From (66), we find that if $[u_1, u_2]^T$ denotes the unit vector for the boundary of the motion cone of a patch at $[x_0, y_0]^T$, then $\mathbf{r} = [x_0 + k u_1, y_0 + k u_2]^T$ for $k \in \mathbb{R}$ is the locus of the patch positions with $[u_1, u_2]^T$ as the boundary of their planar motion cones. ■

An example to illustrate the result of Corollary 4 is given in Figure 4. Note that when the pivot point does not shift significantly, an approximation of the maximum amount of rotation can be achieved by calculating the angle between the direction of \mathbf{v}_h and the stable boundary of the planar motion cone. Knowing the direction of possible displacements of the patch with respect to the object, the result of Theorem 9 makes it possible to answer whether the approximation is an upper bound or a lower bound.

4.4. Pivot point

The pivot point is where the velocity of the hand and the object are the same. The point can be regarded as a temporary joint between the object and the hand, which provides an insight about the motion of the object for a short period of time. If the location of pivot points varies significantly as a result of velocity changes or location of the patch, then the “pivoting joint” approximation will not be sufficient.

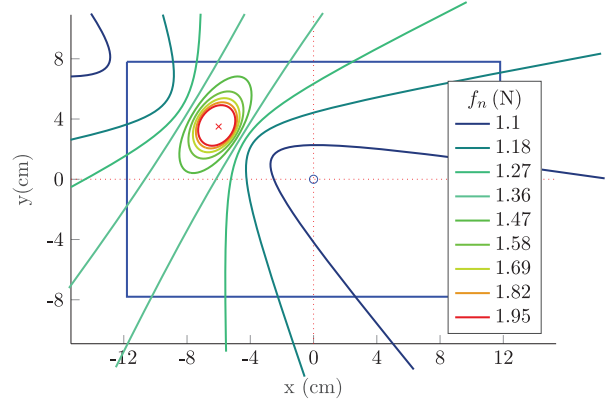


Fig. 5. An example demonstrating the locus of possible pivot points for all hand velocities (see Theorem 10). Each color corresponds to a fixed normal force. For higher normal forces exerted by the hand, the pivot points get closer to the cross, which represents the COP of the friction patch.

Theorem 10. *In a given configuration, the locus of pivot points for all hand velocities is a conic section.*

Proof. The set of possible wrenches \mathbf{w} for pivoting mode lives on the intersection of a cone and the unit sphere according to (22). Transforming this set to \mathbf{v}_{rel} using (25) results into a new cone for relative twists. Since all \mathbf{v}_{rel} on a generatrix of the cone result in the same pivot point, it is enough to consider the intersection of this cone with the plane $\omega_r = 1$ to find x_p and y_p . This completes the proof. ■

According to Theorem 10, the locus of pivot points partitions the space into three regions, which can be mapped to the three modes of the system. For example, assuming the locus is an ellipse, in pivoting mode the pivot points lie on the ellipse. If the hand slips against the object the COR of the hand will be inside the ellipse, while in sticking mode the COR lies outside the ellipse. Figure 5 illustrates the result of Theorem 10 for an example where normal forces are varied. As it can be seen, when the normal force is low the curves are not closed. Then, the pivot point may not lie on the object, and a large portion of the twists can result in slipping mode.

4.5. Stability

The following theorems concern the fixed points of \mathbf{q}_{rel} . These partly correspond to the *sticking* mode, i.e., when the patch configuration does not change with respect to the object, and are analogous to what is referred to in the existing literature as “stable pushing.” Assume now that a straight-line motion starts from pivoting mode. A possible fixed point can be reached at the limit when $\omega_o = 0$. This requires a different notion of stability. First, we examine the properties of sticking mode for achieving stable pushing. Afterwards, the stability of fixed points of the system from a dynamical system perspective is analyzed.

Theorem 11. *The twists for sticking with the largest margin corresponds to the generalized eigenvector of $\hat{\mathbf{A}}$ and \mathbf{B} with the smallest eigenvalue through*

$$\mathbf{v}_h = k\hat{\mathbf{A}}\boldsymbol{\phi}_{\min}, \quad k \in \mathbb{R} \quad (67)$$

Similarly, the twists corresponding to slipping mode with the largest margin can be found using the eigenvector with the largest eigenvalue

$$\mathbf{v}_h = k\hat{\mathbf{A}}\boldsymbol{\phi}_{\max} \quad (68)$$

Proof. According to (35), sticking with the largest margin is obtained at the minimum of

$$c(\mathbf{w}) = \mathbf{w}^T \mathbf{C} \mathbf{w} \quad (69)$$

under the constraint of (33b), that is

$$\mathbf{w}^T \mathbf{w} = 1 \quad (70)$$

Similarly, slipping with the largest margin is obtained at the maximum of (69) under the constraint of (39b), that is

$$\mathbf{w}^T \boldsymbol{\Lambda} \mathbf{w} = 1 \quad (71)$$

Given the facts that \mathbf{C} is diagonal and $\boldsymbol{\Lambda} = \mathbf{C} + \mathbf{I}$, the optimization problems have trivial solutions with \mathbf{w} having only one non-zero element in the row corresponding to the smallest or largest element of $\boldsymbol{\Lambda}$. Applying the relations (33a) and (39a) completes the proof. ■

The amount of sticking margin can be characterized as the minimum external wrench disturbance at the object frame, \mathbf{w}_{dist} , that can cause a mode change from sticking mode. Certainly, the effect of the mode change is more drastic if the system does not have the tendency to go back to sticking mode. This can happen when the \mathbf{v}_h is close to an unstable boundary of the motion cone, which is the subject of Theorem 14.

Theorem 12. *The largest sticking margin is*

$$\mathbf{w}_{\text{dist}} = \sqrt{\left| \frac{\lambda_{\min} - 1}{\lambda_{\max} - 1} \right|} \mathbf{G}^T \boldsymbol{\phi}_{\max} \quad (72)$$

where the smallest and largest generalized eigenvalues of $\hat{\mathbf{A}}$ and \mathbf{B} are denoted by λ_{\min} and λ_{\max} , respectively.

Proof. From the proof of Theorem 11, we know that the largest margin is achieved for \mathbf{w} that is zero except at the row corresponding to λ_{\min} . This ensures that $\mathbf{w}^T \mathbf{C} \mathbf{w} < 0$ is minimized given the constraint that $\|\mathbf{w}\| = 1$. To change the mode of the system, the additional wrench has to fulfill

$$(\mathbf{w} + \Delta \mathbf{w})^T \mathbf{C} (\mathbf{w} + \Delta \mathbf{w}) = 0 \quad (73)$$

Since $\mathbf{C} = \boldsymbol{\Lambda} - \mathbf{I}$ is diagonal, the shortest distance to the cone is simply obtained from

$$(\lambda_{\min} - 1) + \Delta w^2 (\lambda_{\max} - 1) = 0 \quad (74)$$

where Δw is the only non-zero element of $\Delta \mathbf{w}$ corresponding to the largest eigenvalue. Accordingly, the solution is

$$\Delta w = \sqrt{\left| \frac{\lambda_{\min} - 1}{\lambda_{\max} - 1} \right|} \quad (75)$$

The proof is completed by transforming $\Delta \mathbf{w}$ to the object frame using (23). ■

When the velocity of the patch is limited to linear velocities ($\omega_h = 0$), possible wrenches generated by the patch lie on a plane. Consequently, the optimum of (69) must be obtained in that subspace.

Theorem 13. *If the friction is isotropic, for a linear motion, sticking with the largest margin is obtained when the velocity is aligned with the line connecting the COP of the object to the COP of the patch.*

Proof. Minimizing (69) under the constraint (70) is equivalent to minimizing

$$\mathbf{v}_h^T \hat{\mathbf{A}}^{-1} \mathbf{B} \hat{\mathbf{A}}^{-1} \mathbf{v}_h \quad (76)$$

under the constraint

$$\mathbf{v}_h^T \hat{\mathbf{A}}^{-1} \mathbf{v}_h = 1 \quad (77)$$

In addition, limiting to linear motions we must impose

$$\omega_h = 0 \quad (78)$$

Since the friction is assumed to be isotropic, we can reorient \mathcal{O} such that the y -axis points to the COP of the patch. In addition, we align \mathcal{H} with \mathcal{O} . Now assume $\mathbf{A} = \text{diag}([a, a, a_3])$ and $\mathbf{B} = \text{diag}([b, b, b_3])$. Accordingly,

$$\hat{\mathbf{A}} = \mathbf{J} \mathbf{A} \mathbf{J}^T \quad (79)$$

where $\mathbf{J} := \mathbf{J}^T([0, r]^T)$ and r is the distance between the COP of the object and the patch. Since $\omega_h = 0$, for evaluating (76) and (77) only the first two rows and columns of $\hat{\mathbf{A}}^{-1}$ and $\hat{\mathbf{A}}^{-1} \mathbf{B} \hat{\mathbf{A}}^{-1}$ are important. These submatrices are equal to

$$(\hat{\mathbf{A}}^{-1})_{2 \times 2} = \frac{1}{a} \mathbf{I} \quad (80)$$

$$(\hat{\mathbf{A}}^{-1} \mathbf{B} \hat{\mathbf{A}}^{-1})_{2 \times 2} = \frac{b}{a^2} \begin{bmatrix} 1 + \frac{b_3}{b} r^2 & 0 \\ 0 & 1 \end{bmatrix} \quad (81)$$

The minimum of (76) is obtained along the longest axis of the ellipse defined by (81), that is the y -axis. ■

Note that the result of Theorem 13 applies to the case when no angular velocity for the patch is permitted and it is analogous to pulling/pushing results (compare with Theorem 1 of Huang et al. (2017)). However, if angular velocity is allowed, under the same assumption of isotropic frictions, the sticking direction with the largest margin will

be perpendicular to the line passing through the COPs of the object and the patch. This can be confirmed by evaluating (67) or by evaluating the generalized eigenvalues of $\hat{\mathbf{A}}^{-1}$ and \mathbf{B}^{-1} , which gives the solution to (76)–(77).

All the velocities inside the sticking motion cone are fixed points of the system. However, half of the fixed points lying on the surface of the cone are unstable. This is what we intuitively know about pulling versus pushing an object. The next theorem proves this.

Theorem 14. *If a certain twist on the boundary of the motion cone results in a stable fixed point, then the fixed point resulting from the opposite twist is unstable.*

Proof. At a fixed point of the system, the patch will not displace with respect to the object. Accordingly, we first derive the dynamics of the relative pose $\mathbf{q}_{\text{rel}} = \mathbf{R}(-\theta_o)(\mathbf{q}_h - \mathbf{q}_o)$. By taking the derivative of the expression and utilizing (31), we find

$$\begin{aligned}\dot{\mathbf{q}}_{\text{rel}} &= \mathbf{G}^{-1} \mathbf{v}_{\text{rel}} \\ &= \mathbf{G}^{-1} \left(\mathbf{I} + (\alpha \mathbf{B} \hat{\mathbf{A}}^{-1})^{-1} \right)^{-1} \mathbf{v}_h\end{aligned}\quad (82)$$

We linearize the system at the boundary of pivoting and sticking modes, i.e., at $\mathbf{q}_{\text{rel}} = \mathbf{q}_0$ where $\alpha = 0$. The eigenvalues of the linearized system will tell us about stability of fixed points when the system is perturbed away from the sticking region. Denoting the variation in \mathbf{q}_{rel} by $\Delta \mathbf{q}_{\text{rel}}$, the linearized system can be written as

$$\dot{\Delta \mathbf{q}}_{\text{rel}} = \mathbf{M} \Delta \mathbf{q}_{\text{rel}} \quad (83)$$

where

$$\mathbf{M} = \mathbf{G}^{-1}(\mathbf{q}_0) \mathbf{B} \hat{\mathbf{A}}^{-1} \mathbf{v}_h \nabla \alpha \quad (84)$$

Here, we have considered $\alpha = \alpha(x_r, y_r, \theta_r)$, which is the solution of (29).

First, we observe that \mathbf{M} is a matrix of rank 1, since its columns are scaled versions of the same vector. Accordingly, \mathbf{M} has at most one nonzero eigenvalue, which can be expressed as

$$\mathbf{u} := \mathbf{G}^{-1} \mathbf{B} \hat{\mathbf{A}}^{-1} \mathbf{v}_h \quad (85)$$

and the corresponding eigenvalue is

$$\nabla \alpha \mathbf{u} = \left[\frac{\partial \alpha}{\partial x_r}, \frac{\partial \alpha}{\partial y_r}, \frac{\partial \alpha}{\partial \theta_r} \right] \mathbf{u} \quad (86)$$

Note that α is an even function of \mathbf{v}_h , i.e., the solution of (29) is the same for both \mathbf{v}_h and $-\mathbf{v}_h$. Hence, the gradient of α is unaffected by changing the direction of motion while \mathbf{u} according to (85) will be negated. Therefore, we conclude that for opposite twists, the signs of the eigenvalues of the linearized system are different. This implies that if a fixed point resulting from a twist on the boundary of pivoting and sticking regions is stable, the fixed point due to the opposite twist cannot be stable. ■

As it can be concluded from the proof of Theorem 14, the relative position does not have an asymptotic stability. Thus, the patch can gradually drift with respect to the object unless other effects such as changes in the LSs contribute to stabilization. Moreover, to find if a direction of motion is stable, we have to check whether the sign of expression (86) is negative or not. Although it is possible to derive an analytic expression, a practical way is to check what direction the object would rotate toward if it is perturbed away from the fixed point. For linear motions this approach works even if the object is far from the fixed point, since the object rotates always toward a stable fixed point.

5. Experiments and results

In this section, we consider applications of the model developed in previous sections. Specifically, we are interested in using a robotic soft finger to reorient a flat object on a table. This can be done similarly to how a human would manipulate a cell phone on a table, as illustrated in Figure 1.

We performed a number of simulations and robotic experiments to validate the model and its application. The simulations were carried out in Matlab, and the robotic experiments were performed by a Kuka LBR IIWA7 robot.

5.1. Simulations

5.1.1. Hand placement. When a part of the hand is used for reorienting an object, we leverage on the fact that there is a pivot point in the vicinity of the contact region. See Figure 11 for an example of the locus of the pivot point and the origin of the hand frame during sliding motion.

For sliding, the placement of the hand is constrained by:

- the direction and amount of rotation;
- final constraints such as not causing the object to topple at the edge of the surface;
- the weight of the object to avoid flipping it;
- the requirement for pivoting, i.e., the object should not be caged.

If the trajectory of the patch and its final relative pose with respect to the object are given, then there is not much freedom left for the initial placement of the hand. Otherwise, the placement can be optimized for different criteria, such as the shortest distance to achieve a certain rotation or the lowest uncertainty, e.g., by ensuring that the desired pose is a stable fixed point.

When using a linear motion to reorient an object, the upper limit for the amount of object rotation is the angle between the velocity vector of the patch and the line passing through the COPs of the patch and the object, provided that the friction is isotropic and there is no torsional friction (Huang et al., 2017). A more accurate estimation can be obtained by measuring the angle between the velocity vector and the stable boundary of the planar motion cone for a given hand placement. Figure 6 visualizes the amount

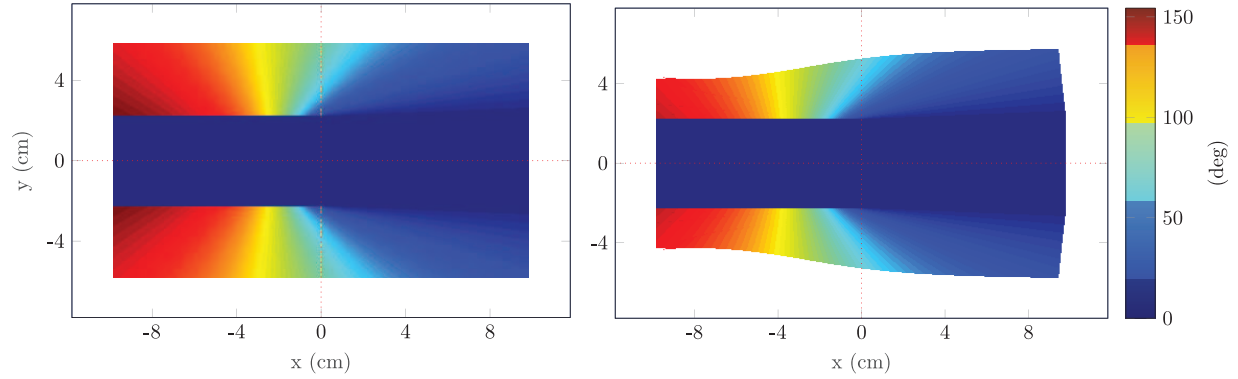


Fig. 6. Visualization of maximum amount of rotation as a function of initial patch location for $\mathbf{v}_h = [1, 0, 0]^T$. On the left, the approximate solution based on the angle between the direction of hand motion and the stable boundary of the motion cone, on the right the final amount of rotation based on simulated sliding. If the hand is initially placed in the white area, the patch will touch an edge of the object or goes outside of the object boundary. In the dark blue area in the middle, the hand and the object stick together.

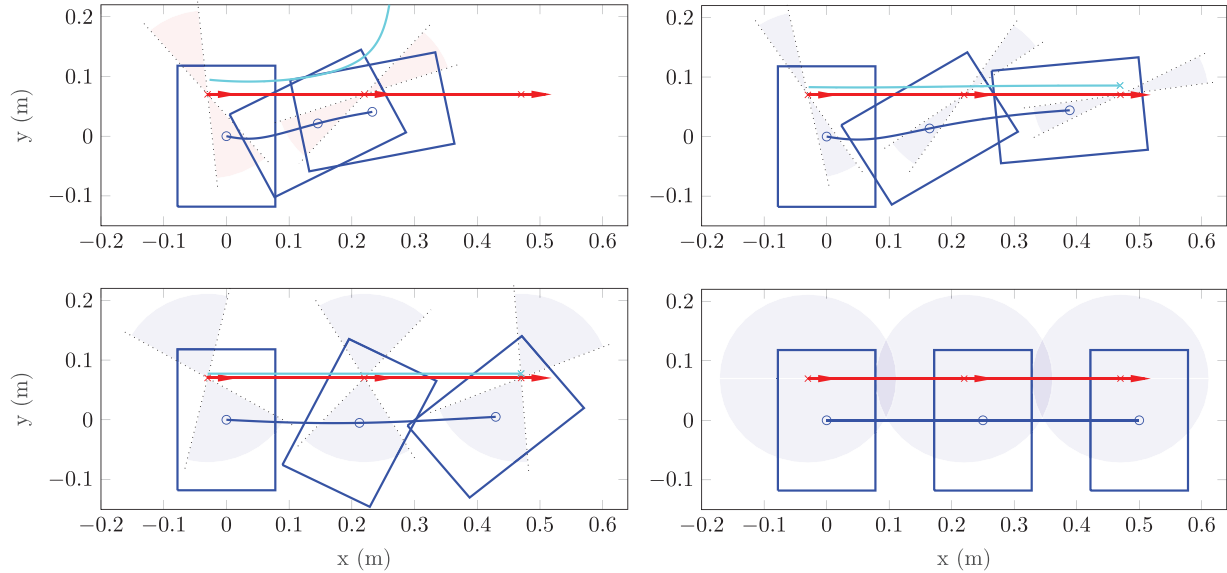


Fig. 7. Sliding an object along a straight line from left to right. The origin of the object frame, the origin of the hand frame and the pivot point are shown in blue, red, and cyan, respectively. The dashed lines represent the boundary of motion cones. The slipping and sticking cones are shaded in light red and light blue, respectively. Considering left–right top–bottom ordering, fixed normal forces 1.43, 1.7, 4, and 6 N are applied, respectively. In the top-left figure, the hand slips after some time completely outside the boundary of the object, while in the bottom-right figure the mode is always sticking because of the increased normal force.

of expected rotation as a function of the initial hand placement from simulation of entire trajectory and compares it with the approximation based on motion cones. As can be concluded from this example, the system behaves as if there was a joint between the object and the hand with a certain maximum limit. This is the case when the normal forces are large enough, but the approximation deteriorates as the normal force is decreased.

5.1.2. Trajectories. We present the results of simulations of the model with the parameters specified here. The box dimensions are $15.6 \text{ cm} \times 23.6 \text{ cm}^2$. The patch is circular with a radius of 2.0 cm. The weight of the box is 450 g. The coefficient of friction between the box and the surface

and the soft finger and the box are $\mu_{oe} = 0.2$ and $\mu_{ho} = 0.8$, respectively. We assume a uniform pressure distribution between the box and the surface when the box is not pressed and a Hertzian pressure distribution for the soft finger. To account for the shift of COP, we use (56) with $c = 0.6$ and $\delta = 2$.

In Figure 7, simulation experiments in which the blue box is being moved from the left to the right by the soft finger are illustrated. The initial placement of the soft finger is $\mathbf{r} = [-3, 7] \text{ cm}$. The end-effector moves at 1 cm/s in the x direction. The simulation runs for 50 seconds. Each subplot corresponds to a certain constant normal force. Considering left–right top–bottom ordering, the normal forces are 1.43, 1.7, 4, and 6 N, respectively. The trajectory of the

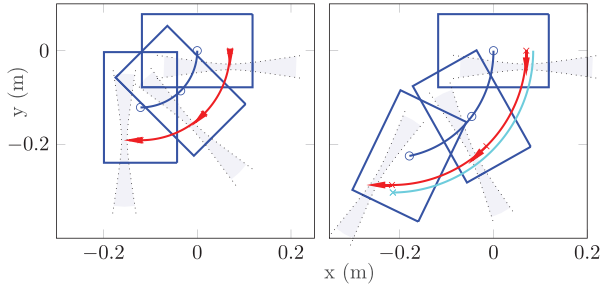


Fig. 8. Sliding an object with $\omega_h \neq 0$. On the left, the tip of the velocity arrow is inside the motion cone, thus the patch sticks to the object. On the right-hand side, the linear velocity has increased and the object is pivoting against the patch.

patch, pivot point, and object are visualized. Note that for generating Figures 4, 5, and 6 presented in previous sections, we have used $f_n = 2.5$ N, $\mathbf{r} = [-3.5, 6]$ cm, and $f_n = 2.5$ N, respectively, while the remaining parameters were set according to the values given in this subsection.

When the soft finger is moving with an angular velocity, the mode depends on the magnitude of the linear velocity. Thus, for the same normal force, angular velocity, and direction of velocity of the finger, different modes might arise. This is because of the fact that when $\omega_h \neq 0$, the modes are no longer mapped to planar cones. Instead, the boundaries of the regions in two dimensions can be represented by the intersection of the motion cone described in Theorem 7 with the plane corresponding to the angular velocity ω_h . Figure 8 shows an example where the finger is rotating at $-\pi/80$ rad/s for 40 seconds. On the left-hand side, the linear velocity is chosen so that it is within the sticking region. In this case, the object is rotated by 90° . On the right, the linear velocity is slightly increased such that it enters the pivoting region, resulting in a faster rotation of the object, exceeding the 90° rotation by the end of the simulation.

5.2. Robotic experiments

The experimental setup consisted of a KUKA lightweight IIWA7 robot arm, with an ATI Gamma force-torque sensor mounted at the wrist. A number of soft fingers were manufactured, and are shown in Figure 13, together with the end-effector of the robot and the object used in the experiments (a hard-cover book). The positions of the robot and of the object were recorded using an Optitrack motion capture system.

5.2.1. Sliding trajectory. To verify the accuracy of the dynamical system presented in Section 3.4, the soft finger mounted at the robot end-effector was pressed against the object and commanded to move at a certain velocity, while maintaining a constant normal force. An image sequence of one trial is shown in Figure 9, with the trajectories of the center of the book overlaid in blue and of the center of the friction patch in red.

An experiment under similar conditions was tested in simulation, calculating the trajectories of the object, finger, and pivot point, and the forces that arise from this interaction. In Figure 10, the full state of the system and the wrenches at the hand frame as a function of time are shown for both simulation (solid) and experimental (dashed) data. To identify **A**, **B**, and *s*, i.e., the percentage of the shift of COP due to loading, we set up an optimization problem that minimizes the error between the simulated experiment and the measured data. The hand velocity and the normal forces are chosen as the average of the respective values from the experiments. A comparison between the simulated and the experimental results is shown in Figure 11. The plot on the left shows the simulated object path in blue and the experimental in dashed black. The plot on the right-hand side of Figure 11 shows the positions of the patch and the pivot point in the object frame. It can be seen that the model accurately describes the sliding motion of the object, reaching similar positions and orientations within the same amount of time. In Figure 12, a number of sample sliding motions are shown. The same parameters, except for the COP of the patch which could vary slightly from an experiment to another, are used for all the simulated results. The prediction of the proposed model matches with the experimental results, with a root-mean-square (RMS) error across all experiments of 3.8 mm in position and 0.0148 rad in orientation.

5.2.2. Modes and motion cones. Validation of the motion cones and possible modes was carried out by placing the soft finger at different locations on the book and performing linear motions in various directions, with zero angular velocity, while maintaining a constant normal force. The angular velocity of the object was recorded and is visualized in Figure 14 for two different locations. The symmetry presented in these results confirm what is posited in Corollary 1. The left-hand side of the figure shows the angular velocities when pressing the soft finger with a normal force of 6 N. Since the friction is approximately isotropic, according to Theorem 13 the soft finger sticks to the object when moving towards or away from the COP of the object. When moving perpendicularly to this line, the object pivots and has some rotational velocity. The right-hand side shows the same effect with a normal force of 2 N. The patch slips against the object when moving along a direction close to the line that passes through the COPs of the object and of the patch and pivots when the velocity is perpendicular to that.

5.2.3. Controlled sliding. If the goal is to rotate the object to a desired orientation on the edge of a table, we know from the dynamical system described in Section 3.4, that only two out of the three following quantities can be controlled simultaneously: (i) normal force; (ii) velocity of the

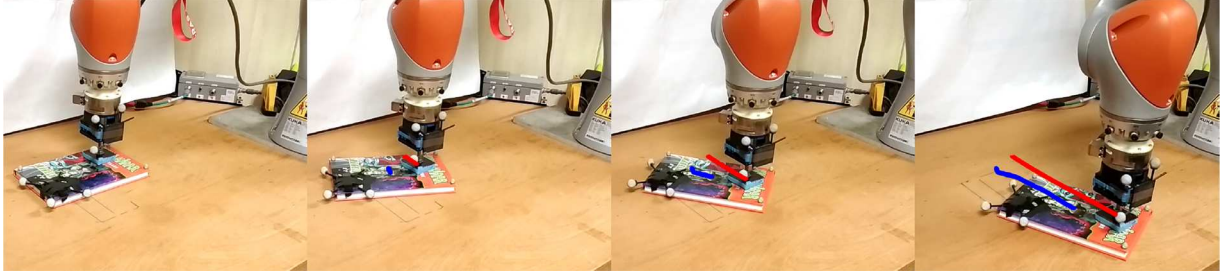


Fig. 9. Sliding motion experiment: a soft finger is attached to the KUKA LBR IIWA7 robot. The book is being dragged toward the edge. Trajectories of the center of the object are shown in blue and of the friction patch in red.

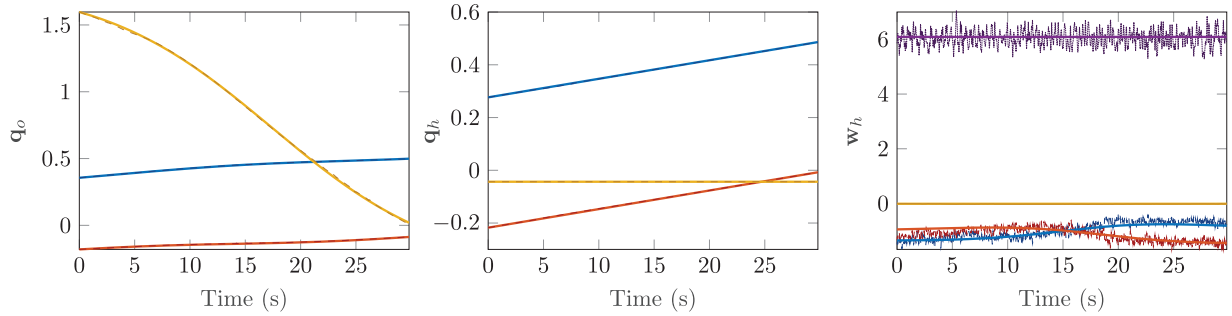


Fig. 10. A sample of poses and forces in pivoting mode during a straight-line motion. The three components of each vector are shown in blue, red, and yellow colors, respectively. The normal force at the hand frame has additionally been shown in w_h plot in violet. Dashed lines represent the experimental results, which are almost indistinguishable from the simulation.

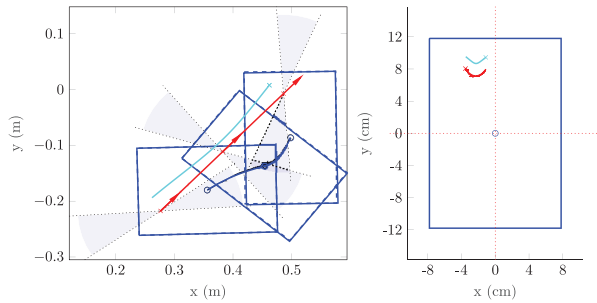


Fig. 11. Comparison of simulated and experimental results for a straight-line pivoting motion. On the left, the rectangles in blue illustrate simulation, and in dashed black experimental results. On the right, the locus of the origin of the patch frame (red) and the pivot point (cyan) with respect to the object are shown. The crosses mark the start of the motion. In this example, it is almost a perfect match between the simulation and the robot experiment.

hand; (iii) the position of the pivot point. Moreover, possible feedback signals for a controller are w_h , v_o , q_o , and q_{rel} .

A possible strategy can then be to place the hand where a straight trajectory with a constant normal force results at a stable fixed point at the desired orientation for a long enough surface. This approach may not be realistic, since the friction properties are usually difficult to determine accurately, as they may vary along the sliding surface (Yu et al., 2016).

A more robust way to achieve this is to select a hand placement that can clearly rotate the object to the desired orientation, and then use feedback from the actual angle of the object to adjust the rotation of the object by regulating the normal force applied by the soft finger. Other considerations can be made, such as not having the finger too close to the border of the object, since their relative position may change during motion, or placing the finger such that, when the object reaches the edge, it does not topple it. We may first keep the normal force at a minimum amount required to stop object rotation. Then, during the execution of the trajectory, if the angular velocity needs to be increased, the robot can reduce the normal force to allow this rotation. This control law can be implemented through a simple proportional controller as

$$f_n = -K \text{sat}(\theta_{\text{ref}} - \theta_{\text{meas}}) + f_U \quad (87)$$

where θ_{ref} is the reference angle and f_U an upper limit for the normal force, which can be obtained from the model, $\text{sat}(\cdot)$ is the saturation function with tunable upper and lower limits, and K is the proportional gain.

A lower bound for the normal force can be chosen such that there will be no slipping mode and a fixed point, i.e., switching to the sticking mode is guaranteed. More advanced schemes might include an integral action to reduce the sensitivity to f_U , and a feedforward term.

Given a patch location and a velocity direction, a reference trajectory for θ_o can be defined, as long as it stays

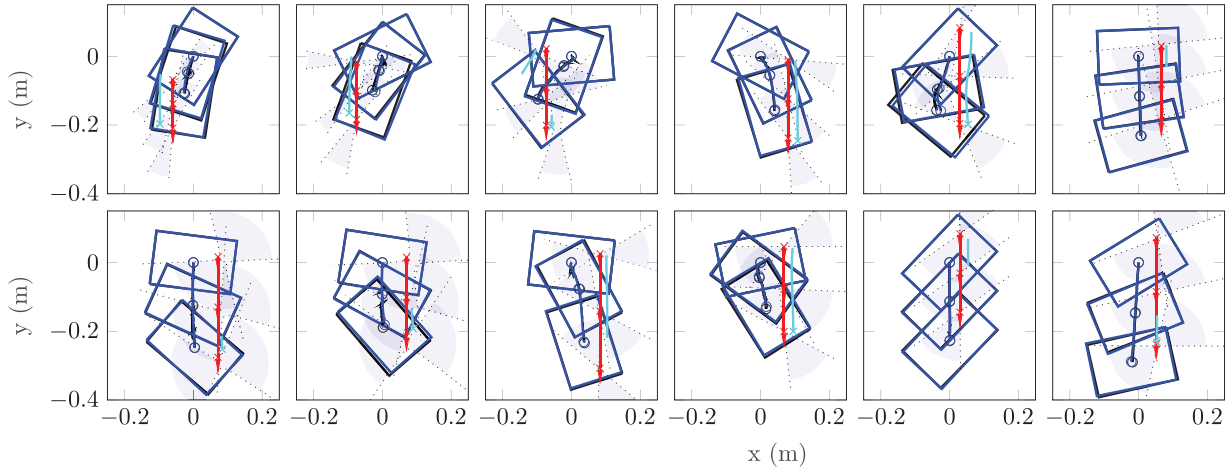


Fig. 12. Samples of sliding motion illustrating paths and motion cones. Blue: modeled; black: experimental; red: friction patch; cyan: pivot point. The soft finger moves from top to bottom in all experiments, while the initial configuration of the book is varied for each experiment. Considering left-right top-bottom ordering, fixed normal forces (1–3: 5 N, 4–5: 6 N, 6–11: 8 N; and 12: 10 N) are maintained during each experiment. In subfigures 3, 6, 7, 8, and 12, the finger has an angular velocity.



Fig. 13. Experimental setup. From left to right: robot end-effector with optical markers, spherical and square soft fingers, and the object (book) with optical markers.

within the calculated limits as in Figure 6. Figure 15 illustrates the result of an experiment for tracking a desired trajectory of the object orientation control law (87). This simple proportional controller was able to closely track the reference trajectory, applying larger normal forces to keep the object from rotating, and relaxing the pressure whenever faster rotation was required.

6. Discussion

The experimental results suggest a good match between theory and practice. The assumptions of quasi-static motion and ellipsoid approximation of LSs hold in our experiments. However, when the contact areas are not negligible, an accurate estimation of the location of COPs becomes important. Accordingly, due to variability in the pressure distribution and friction coefficients (Yu et al., 2016), applying nominal values may not be adequate and, hence, feedback must be employed.

A frictional patch allows both pulling and pushing of an object. Compared with pushing scenarios (Mason, 1982;

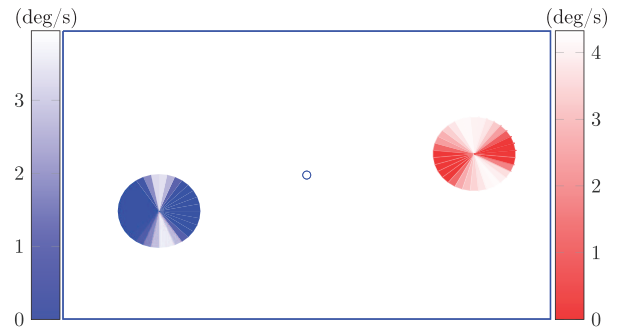


Fig. 14. Visualization of the sticking and pivoting cones (blue, $f_n = 6$ N) and slipping and pivoting cones (red, $f_n = 2$ N) based on $|\omega_o|$ as a result of moving the soft finger with 1 cm/s in various directions.

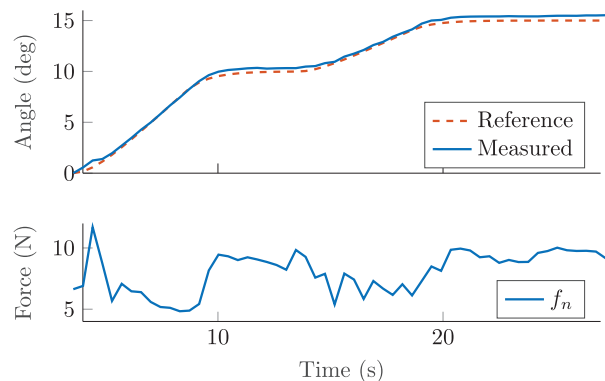


Fig. 15. Experimental result of tracking a reference trajectory for the object orientation.

Zhou and Mason, 2017), we observe that the torsional friction adds some stability margin for pushing. Nevertheless, reversing from a stable motion at the border of the pivoting region is unstable and sensitive to small perturbations. In addition, at the stable fixed point, the center of a circular patch would not align with the COP of the object, in contrast to the scenario where there is no torsional friction considered by Huang et al. (2017). Another observation is that, if the friction is anisotropic, the main axis of the motion cone corresponding to sticking mode is not directed toward the COP of the object.

A fundamental difference between our model and previous studies based on pulling/pushing is the inclusion of torsional friction. Since the torsional friction can be regulated by adjusting the normal force, we have in effect an extra degree of actuation besides the motion of the hand. This fact has been successfully utilized in the trajectory tracking experiment in Section 5.2.3. The reason that a simple controller such as (87) can work in practice is that for a given velocity of the patch, the angular velocity of the object (ω_o) could be approximated as a linear function of f_n around a working point.

For a linear motion and a fixed normal force, the distance to cause a certain amount of rotation in the object is independent of the velocity of the patch. Moreover, by increasing the normal force, the motion cone widens and, hence, the maximum possible rotation is reduced. At the same time, the object rotates slower, which results in a longer distance to achieve a certain amount of rotation.

According to Theorem 11, the generalized eigenvectors of $\hat{\mathbf{A}}$ and \mathbf{B} can be interpreted as the *principal sliding wrenches*, while the generalized eigenvectors of $\hat{\mathbf{A}}^{-1}$ and \mathbf{B}^{-1} define *principal sliding twists*. These eigenvectors and their corresponding eigenvalues provide important information for a sliding motion at a given configuration. Specifically, the eigenvectors characterize wrenches and twists that cause sticking and slipping with largest margins.

The approximation method developed in Appendix A can be viewed as an extension of the pushing model by Zhou et al. (2017); Zhou and Mason (2017), where the pusher can also exert torsional friction, and the ellipsoidal LSs are given in their most generic form. If the pivot point is additionally allowed to displace, the model for planar sliding using friction patches is recovered. As explained in Appendix A, the displacement of the pivot point can be accounted for in the approximate solution in an iterative fashion.

If the stiffness of the material in contact with the slider is low, we cannot assume the velocity of the patch as a control input anymore. However, for many practical applications the deflection of the soft finger with respect to the overall motion of the object is negligible. A possible extension is to augment the Coulomb friction model of the patch with a spring-damper model to account for the flexibility of the soft finger. This approach is somewhat similar to the work by Kao and Cutkosky (1992), although they do not derive

any dynamical system for the time evolution of the system. In extreme scenarios, it may not even be possible to represent the velocity field of a soft finger by the rigid part of the velocity of the patch. Consequently, discretization of the contact surface or approaches based on the continuum mechanics should be considered.

A more realistic friction model should be able to distinguish between static and dynamic friction coefficients. Moreover, higher-order approximation of LS proposed by Zhou et al. (2018) can be adapted to our approach, although there may not exist efficient algorithms to solve the resulting systems of equation.

A control algorithm can benefit from haptic exploration for identification of the friction properties of the object being manipulated. For example, by adjusting the normal force and measuring tangential forces, it is possible to distinguish if the soft finger slides *with the object* or *on the object*. Such ideas can be incorporated for identification and control of the mode of the system.

Using the developed model, several planning problems can be formulated and solved. A possible planning problem is to find trajectories to slide an object from an initial to a desired pose such that the contact between surfaces is maintained and the normal force is within desired limits. Another example is to find minimal required normal forces to slide an object along a path without pivoting or slipping. Note that when the pivot point varies significantly, a simple approximation of the dynamics as an object with a joint is not sufficient. In such scenarios, a more elaborate dynamical system as that presented in this article must be considered.

7. Conclusions

A mathematical model for planar sliding has been provided, where the friction between a soft finger and the slider generates forces for the motion of the object. The concept of motion cones is extended to find criteria for three modes of the system, namely sticking, slipping, and pivoting. In pivoting mode, the soft finger can be regarded as if it is connected to the slider using a joint, which in general slides on the surface of the object. This interconnection enables both pushing and pulling of the object.

We have relaxed some of the common assumptions made for modeling frictional contacts such as diagonal matrices for approximating LSs or having a fixed pivot point. The result of modeling is a hybrid dynamical system, which is used for finding fixed points of the system and determining their stability.

The developed model can be used as the basis for planning and control design. For example, it makes it possible to predict the directions for stable sliding with the largest margin, to approximate the amount of rotation before reaching a fixed point, to predict whether the contact is maintained or the soft finger would go off the surface of the object, etc.

We evaluate the model experimentally. The comparison of the results with the simulated model suggests that the essential physical factors are captured in the model. In addition, we demonstrate the possibility of tracking a desired trajectory by regulating normal forces based on visual feedback.

In the future, we consider designing adaptive and robust controllers to deal with the variations in the parameters of the system during sliding.

Acknowledgements


The authors would like to thank Maria Lazzaroni and Lorenza Mancini for their assistance in carrying out the force-plate experiment.

Funding

The authors disclosed receipt of the following financial support for the research, authorship, and/or publication of this article: The research has received funding from the SOMA project (European Commission, Horizon 2020 Framework Programme, grant number H2020-ICT-645599).

ORCID iDs

M. Mahdi Ghazaei Ardakani  <http://orcid.org/0000-0002-4713-1003>

Joao Bimbo  <http://orcid.org/0000-0002-4720-9026>

References

- Bicchi A, Salisbury KJ and Brock DL (1993) Experimental evaluation of friction characteristics with an articulated robotic hand. In: Chatila R and Hirzinger G (eds.) *Experimental Robotics II*. Berlin: Springer, pp. 153–167.
- Chavan-Dafle N, Holladay R and Rodriguez A (2018) In-hand manipulation via motion cones. In: *Proceedings of Robotics: Science and Systems (RSS) XIV*, Pennsylvania, PA.
- Chavan-Dafle N and Rodriguez A (2017) Stable prehensile pushing: In-hand manipulation with alternating sticking contacts. *arXiv preprint arXiv:1710.11097*.
- Fakhari A, Keshmiri M and Kao I (2016) Development of realistic pressure distribution and friction limit surface for soft-finger contact interface of robotic hands. *Journal of Intelligent and Robotic Systems* 82(1): 39–50.
- Featherstone R (2008) *Rigid Body Dynamics Algorithms*. New York: Springer, pp. 37–38.
- Goyal S (1989) *Planar Sliding of a Rigid Body with Dry Friction: Limit Surfaces and Dynamics of Motion*. PhD Thesis, Cornell University, Ithaca, NY.
- Hou Y, Jia Z, Johnson AM and Mason MT (2016) Robust planar dynamic pivoting by regulating inertial and grip forces. In: *Proceedings of the International Workshop on the Algorithmic Foundations of Robotics*.
- Howe RD and Cutkosky MR (1996) Practical force-motion models for sliding manipulation. *The International Journal of Robotics Research* 15(6): 557–572.
- Howe RD, Kao I and Cutkosky MR (1988) The sliding of robot fingers under combined torsion and shear loading. In: *Proceedings 1988 IEEE International Conference on Robotics and Automation (ICRA)*, pp. 103–105.
- Huang E, Bhatia A, Boots B and Mason M (2017) Exact bounds on the contact driven motion of a sliding object, with applications to robotic pulling. In: *Proceedings of Robotics: Science and Systems (RSS) XIII*, Cambridge, MA.
- Johnson KL (1985) *Normal Contact of Elastic Solids – Hertz Theory*. Cambridge: Cambridge University Press, pp. 84–106.
- Kao I and Cutkosky MR (1992) Quasistatic manipulation with compliance and sliding. *The International Journal of Robotics Research* 11(1): 20–40.
- Kao I and Cutkosky MR (1993) Comparison of theoretical and experimental force/motion trajectories for dextrous manipulation with sliding. *The International Journal of Robotics Research* 12(6): 529–534.
- Lynch KM, Maekawa H and Tanie K (1992) Manipulation and active sensing by pushing using tactile feedback. In: *Proceedings IEEE/RSJ International Conference on Intelligent Robots and Systems (IROS)*, pp. 416–421.
- Lynch KM and Mason MT (1996) Stable pushing: Mechanics, controllability, and planning. *The International Journal of Robotics Research* 15(6): 533–556.
- Malvezzi M, Salvietti G and Prattichizzo D (2019) Evaluation of grasp stiffness in underactuated compliant hands exploiting environment constraints. In: Arakelian V and Wenger P (eds.) *ROMANSY 22–Robot Design, Dynamics and Control*. Cham: Springer, pp. 409–416.
- Mason MT (1982) *Manipulator Grasping and Pushing Operations*. PhD Thesis, Massachusetts Institute of Technology, Cambridge, MA.
- Mason MT (1986) Mechanics and planning of manipulator pushing operations. *The International Journal of Robotics Research* 5(3): 53–71.
- Peshkin M and Sanderson A (1987) Planning robotic manipulation strategies for sliding objects. In: *Proceedings 1987 IEEE International Conference on Robotics and Automation (ICRA)*, pp. 696–701.
- Ruiz-Ugalde F, Cheng G and Beetz M (2011) Fast adaptation for effect-aware pushing. In: *Proceedings 11th IEEE-RAS International Conference on Humanoid Robots (Humanoids)*, pp. 614–621.
- Shi J, Woodruff Ja, Umbanhowar PB and Lynch KM (2017) Dynamic in-hand sliding manipulation. *IEEE Transactions on Robotics* 33(4): 778–795.
- Viña B FE, Karayiannidis Y, Smith C and Kragic D (2016) Adaptive control for pivoting with visual and tactile feedback. In: *Proceedings IEEE International Conference on Robotics and Automation (ICRA)*, pp. 399–406.
- Xue Y and Kao I (1994) Dexterous sliding manipulating using soft fingertips. In: *Proceedings IEEE International Conference on Robotics and Automation (ICRA)*, pp. 3397–3402.
- Xydas N and Kao I (1999) Modeling of contact mechanics and friction limit surfaces for soft fingers in robotics, with experimental results. *The International Journal of Robotics Research* 18(9): 941–950.
- Yu KT, Bauza M, Fazeli N and Rodriguez A (2016) More than a million ways to be pushed. A high-fidelity experimental dataset

of planar pushing. In: *Proceedings 2016 IEEE/RSJ International Conference on Intelligent Robots and Systems (IROS)*, pp. 30–37.

Zhou J, Bagnell JA and Mason MT (2017) A fast stochastic contact model for planar pushing and grasping: Theory and experimental validation. In: *Proceedings of Robotics: Science and Systems XIII*, Cambridge, MA.

Zhou J and Mason MT (2017) Pushing revisited: Differential flatness, trajectory planning and stabilization. In: *Proceedings of the International Symposium on Robotics Research (ISRR)*.

Zhou J, Mason MT, Paolini R and Bagnell D (2018) A convex polynomial model for planar sliding mechanics: theory, application, and experimental validation. *The International Journal of Robotics Research* 37(2–3): 249–265.

Appendix A. Approximate solution

The approximate solution has to solve the same set of equations as in Section 3.2, i.e., (22) and (24)–(26), but we relax some of the constraints assuming a known estimate of the pivot point. In practice, having such an estimate is realistic, since it is desired to keep the pivot point close the center of the patch. Moreover, we can devise an iterative algorithm to update the position of the pivot point in order to improve the accuracy of the solution.

The condition for the pivot point can be expressed as

$$\mathbf{J}_p \mathbf{v}_{\text{rel}} = 0 \quad (88)$$

where $\mathbf{J}_p \in \mathbb{R}^{2 \times 3}$ corresponds to the first two rows of $\mathbf{J}(\mathbf{p})$, which is the Jacobian of the position of the presumed pivot point \mathbf{p} defined in the hand coordinate. Using the definition of \mathbf{v}_{rel} in (26), combined with (24), we find

$$\mathbf{J}_p \hat{\mathbf{A}} \Phi \mathbf{w} = -\frac{\mathbf{v}_p}{k_1} \quad (89)$$

where we have defined $\mathbf{v}_p := \mathbf{J}_p \mathbf{v}_h$.

Considering (89), the general solution for \mathbf{w} given \mathbf{v}_p is

$$\mathbf{w} = -\frac{1}{k_1} \Phi^T \left(\mathbf{J}_p^\dagger \mathbf{v}_p + \gamma \mathbf{n} \right) \quad (90)$$

where $\mathbf{n} = [y_p, -x_p, 1]^T$ spans the nullspace of \mathbf{J}_p and $\gamma \in \mathbb{R}$ is an arbitrary constant. By introducing $\bar{\mathbf{w}} := \Phi^T \mathbf{J}_p^\dagger \mathbf{v}_p$ and $\mathbf{w}_0 := \Phi^T \mathbf{n}$, we rewrite (90) as

$$\mathbf{w} = -\frac{1}{k_1} (\bar{\mathbf{w}} + \gamma \mathbf{w}_0) \quad (91)$$

Note that \mathbf{J}_p is a function of the pivot point and, hence, \mathbf{w} .

Substituting (91) into (22a) results in

$$\gamma^2 \mathbf{w}_0^T \mathbf{C} \mathbf{w}_0 + 2\gamma \mathbf{w}_0^T \mathbf{C} \bar{\mathbf{w}} + \bar{\mathbf{w}}^T \mathbf{C} \bar{\mathbf{w}} = 0 \quad (92)$$

where we have used the facts that $k_1 > 0$ and \mathbf{C} is diagonal. From (92), we can solve for

$$\gamma = \frac{-\mathbf{w}_0^T \mathbf{C} \bar{\mathbf{w}} \pm \sqrt{\Delta}}{\mathbf{w}_0^T \mathbf{C} \mathbf{w}_0} \quad (93)$$

where

$$\Delta := (\mathbf{w}_0^T \mathbf{C} \bar{\mathbf{w}})^2 - (\mathbf{w}_0^T \mathbf{C} \mathbf{w}_0) (\bar{\mathbf{w}}^T \mathbf{C} \bar{\mathbf{w}}) \quad (94)$$

After determining γ , we can substitute (91) into (22b) to find k_1 . Consequently,

$$k_1 = \|\bar{\mathbf{w}} + \gamma \mathbf{w}_0\| \quad (95)$$

Moreover, irrespective of k_1 , by putting \mathbf{w} back to (24) it is possible to conclude

$$\mathbf{v}_o = \mathbf{G}^{-1} \left(\mathbf{J}_p^\dagger \mathbf{J}_p \mathbf{v}_h + \gamma \mathbf{n} \right) \quad (96)$$

where the pivot point and γ depend on the friction parameters and \mathbf{v}_h . Also using (19), we obtain

$$\omega_r = \frac{\mathbf{n}^T \mathbf{v}_h}{\|\mathbf{n}\|^2} + \gamma \quad (97)$$

So far, we have ignored Equation (25). From this equation, we find

$$k_2 = -\frac{\omega_r}{[0, 0, 1] \mathbf{B} \Phi \mathbf{w}} \quad (98)$$

There are two solutions to (92). Using Equation (98), we choose the one which results in a positive value for k_2 . Now, we can calculate \mathbf{v}_{rel} from (25) and use (32) to update the pivot point.

Note that by choosing the frame of the hand at the pivot point, the relation simplifies to

$$\mathbf{v}_o = \mathbf{G}^{-1} \begin{bmatrix} v_{hx} \\ v_{hy} \\ \gamma \end{bmatrix} \quad (99)$$

In this case, the angular velocity of the object is equal to γ .

Other possibility that we can study using this formulation is when there is a fixed amount or no torsional friction. In this case, Equation (22a) must be replaced by

$$\mathbf{w}_0^T \mathbf{w} = m_p \quad (100)$$

which is concluded by transferring wrenches according to (5). Subsequently, we substitute (91) into (100) to obtain

$$\gamma \mathbf{w}_0^T \mathbf{w}_0 = -\mathbf{w}_0^T \bar{\mathbf{w}} - k_1 m_p \quad (101)$$

If $m_p \neq 0$, Equation (101) can be solved together with (95) which results in a quadratic equation. However, if $m_p = 0$ we find immediately

$$\gamma = -\frac{\mathbf{w}_0^T \bar{\mathbf{w}}}{\|\mathbf{w}_0\|^2} = \frac{\mathbf{n}^T \hat{\mathbf{A}}^{-1} \mathbf{J}_p^\dagger \mathbf{v}_p}{\mathbf{n}^T \hat{\mathbf{A}}^{-1} \mathbf{n}} \quad (102)$$

This result reveals the connection to pulling/pushing scenarios in which there is no torsional friction at the pivot point.

Appendix B. Proof of Theorem 2

Proof. Since matrix \mathbf{A} is symmetric, it has six unique elements. Accordingly, by expanding the right-hand side of (13), we find six equations and six unknowns, i.e., the diagonal elements of $\mathbf{\Lambda}$, the angle of rotation θ for $\mathbf{R} := \mathbf{R}(\theta)$, and the vector $\mathbf{r} = [x_r, y_r]^T$ for the Jacobian $\mathbf{J} := \mathbf{J}(\mathbf{r})$. To show that this equation system can indeed be solved, we construct the solution.

Using the elements of \mathbf{A} , we calculate

$$\begin{aligned} x &:= (a_{11} - a_{22}) + \frac{1}{a_{33}}(a_{23}^2 - a_{13}^2) \\ &= (\lambda_1 - \lambda_2) \cos(2\theta) \end{aligned} \quad (103a)$$

$$\begin{aligned} y &:= -2(a_{21} - \frac{1}{a_{33}}a_{13}a_{23}) \\ &= (\lambda_1 - \lambda_2) \sin(2\theta) \end{aligned} \quad (103b)$$

Accordingly, we find

$$\theta = \frac{1}{2} \text{Atan2}(x, y) \text{sign}(\lambda_1 - \lambda_2) \quad (104)$$

If $\lambda_1 \neq \lambda_2$, and we decide a specific ordering for the elements of $\mathbf{\Lambda}$, e.g., $\lambda_1 > \lambda_2$, the angle is uniquely determined. If $\lambda_1 = \lambda_2$, any angle can be chosen including 0.

After finding θ , as an intermediate step we calculate

$$\tilde{\mathbf{\Lambda}} = \mathbf{R}(\theta) \mathbf{A} \mathbf{R}^T(\theta) \quad (105)$$

Now, the elements of \mathbf{r} are obtained as

$$x_r = \frac{\tilde{\Lambda}_{23}}{\tilde{\Lambda}_{33}}, \quad y_r = -\frac{\tilde{\Lambda}_{13}}{\tilde{\Lambda}_{33}} \quad (106)$$

Finally,

$$\mathbf{\Lambda} = \mathbf{J}(-\mathbf{r}) \tilde{\mathbf{\Lambda}} \mathbf{J}^T(-\mathbf{r}) \quad (107)$$

Appendix C. Proof of Theorem 3

Proof. We prove the theorem by contradiction. Assume that there are two distinct positive solutions $\alpha_2 > \alpha_1 > 0$. We prove that this implies that $\mathbf{v}_h = \mathbf{0}$.

Since $\hat{\mathbf{A}}$ and \mathbf{B} are positive-definite, so is $\mathbf{\Lambda}$, and hence all $\lambda_i > 0$, $i \in \{1, 2, 3\}$. The coefficients c_i , which are the diagonal of $\mathbf{C} = \mathbf{\Lambda} - \mathbf{I}$, cannot all have the same sign. Otherwise, the left-hand side of (29) will be irrespective of \mathbf{v}_h either positive or negative and there will be no solution to the equation. This implies that one or two eigenvalues are less than one, while the rest are/is larger than one. Here, we consider the case where $\lambda_1 > 1 > \lambda_2 > \lambda_3$. Other cases are proven similarly.

For α_i , $i \in \{1, 2\}$, we have

$$c_1 \left(\frac{\tilde{v}_{xh}}{\alpha_i \lambda_1 + 1} \right)^2 + c_2 \left(\frac{\tilde{v}_{yh}}{\alpha_i \lambda_2 + 1} \right)^2 + c_3 \left(\frac{\tilde{\omega}_h}{\alpha_i \lambda_3 + 1} \right)^2 = 0$$

We multiply the equation associated with α_i by

$$(\alpha_i \lambda_1 + 1)^2 \quad (108)$$

and subtract the resulting equations from each other to eliminate the first term. Accordingly,

$$c_2 \tilde{v}_{yh}^2 (f_{1,2}(\alpha_2) - f_{1,2}(\alpha_1)) + c_3 \tilde{\omega}_h^2 (f_{1,3}(\alpha_2) - f_{1,3}(\alpha_1)) = 0 \quad (109)$$

where

$$f_{ij}(\alpha) := \left(\frac{\alpha \lambda_i + 1}{\alpha \lambda_j + 1} \right)^2 \quad (110)$$

For $\alpha \geq 0$ and positive values of λ_i , from the derivate of (110) we find that the function is monotonically increasing or decreasing, depending on the sign of $\lambda_i - \lambda_j$. Thus, given our assumptions about λ_i , both $f_{1,2}$ and $f_{1,3}$ are increasing functions. Taking this fact into account, the left-hand side of (109) is always negative unless both \tilde{v}_{yh} and $\tilde{\omega}_h$ are zero. If this is the case, from (29) we conclude that \tilde{v}_{xh} must also be zero. Since \mathbf{v}_h is assumed to be non-zero, this completes the proof by contradiction. ■

Appendix D. Proof of Theorem 4

Proof. First, we show that it is impossible to have no active modes, i.e., there is at least one active mode. Second, we prove that it is impossible to have any two modes active at the same unless $\mathbf{v}_h = \mathbf{0}$.

Let us define

$$f(\beta, \gamma) := \mathbf{w}(\beta, \gamma)^T \mathbf{C} \mathbf{w}(\beta, \gamma) \quad (111)$$

where $\mathbf{w}(\beta, \gamma) = (\beta \mathbf{I} + \gamma \mathbf{\Lambda})^{-1} \tilde{\mathbf{v}}_h$. If neither sticking mode nor slipping mode is possible, from conditions (37) and (41), we conclude

$$f(\beta, 0) > 0 \quad (112a)$$

$$f(0, \gamma) < 0 \quad (112b)$$

Also define $g(\alpha) := f(1, \alpha)$. According to (111), $\text{sign } f(\beta, \gamma) = \text{sign } g(\gamma/\beta)$. Consequently, conditions (112) can be written as

$$g(0) > 0$$

and for a large enough α

$$g(\alpha) < 0$$

Since $g(\cdot)$ is a continuous function, there must exist an $\alpha > 0$ such that $g(\alpha) = 0$, i.e., there is a solution in pivoting mode. Therefore, it is impossible to have no active mode.

For ease of reference, here we summarize (37), (28), and (41), which provide the criteria for sticking, pivoting, and slipping modes, respectively,

$$\tilde{\mathbf{v}}_h^T \mathbf{C} \tilde{\mathbf{v}}_h \leq 0 \quad (113a)$$

$$\alpha > 0, \quad \tilde{\mathbf{v}}_h^T \mathbf{C} (\mathbf{I} + \alpha \mathbf{\Lambda})^{-2} \tilde{\mathbf{v}}_h = 0 \quad (113b)$$

$$\tilde{\mathbf{v}}_h^T \mathbf{C} \mathbf{\Lambda}^{-2} \tilde{\mathbf{v}}_h \geq 0 \quad (113c)$$

Now assume that any pair of these conditions hold true. We can show that this results in a contradiction unless $\mathbf{v}_h = \mathbf{0}$. The proof construction is similar to the proof of Theorem 3 given in Appendix C. More specifically, the term corresponding to the largest eigenvalue is eliminated by multiplying the expressions by proper coefficients similar to (108). Here, we provide the details only for the case where (113a) and (113c) are assumed true.

We know that the diagonal elements of $\mathbf{C} = \mathbf{\Lambda} - \mathbf{I}$ cannot have the same sign. Let us assume $\lambda_1 > 1 > \lambda_2 > \lambda_3 > 0$. Accordingly,

$$\begin{aligned} \lambda_1^2 \tilde{\mathbf{v}}_h^T \mathbf{C} \mathbf{\Lambda}^{-2} \tilde{\mathbf{v}}_h - \tilde{\mathbf{v}}_h^T \mathbf{C} \tilde{\mathbf{v}}_h &= c_2 \tilde{v}_{yh}^2 \left(\left(\frac{\lambda_1}{\lambda_2} \right)^2 - 1 \right) \\ &+ c_3 \tilde{\omega}_h^2 \left(\left(\frac{\lambda_1}{\lambda_3} \right)^2 - 1 \right) \leq 0 \end{aligned} \quad (114)$$

Unless \tilde{v}_{yh} and $\tilde{\omega}_h$ are zero, Equation (114) is strictly negative. However, to fulfill (113a) if $\tilde{v}_{yh} = \tilde{\omega}_h = 0$, \mathbf{v}_h must also be zero since $c_1 > 0$. Thus, we conclude that if $\mathbf{v}_h \neq \mathbf{0}$, then

$$\tilde{\mathbf{v}}_h^T \mathbf{C} \tilde{\mathbf{v}}_h > \lambda_1^2 \tilde{\mathbf{v}}_h^T \mathbf{C} \mathbf{\Lambda}^{-2} \tilde{\mathbf{v}}_h \quad (115)$$

which contradicts the assumption that the left-hand side is less than or equal to zero and the right-hand side is greater or equal to zero. Other scenarios for λ_i are proven similarly. ■

Appendix E. Experimental validation of shift of COP

To understand the effect of loading an object with a given normal force, in terms of the amount of displacement of the COP of the object towards the COP of the patch, a number of experiments were carried out. We used a BTS Force

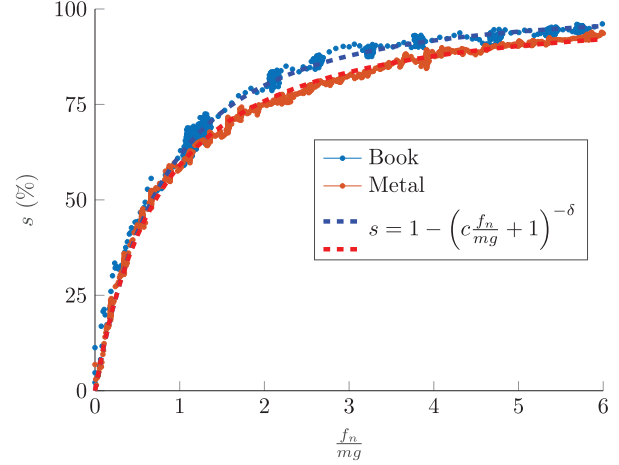


Fig. 16. Experimental results of the effect of normal force in the shift of the object COP towards the patch.

Plate, which measures forces and COPs. The objects were placed on the surface and pressed with an increasing normal force. The shift s (in percentage) is plotted in Figure 16, against the normal force (normalized for object weight) for two different objects: a hardcover book of 463 g, and a flat steel slab of 1,593 g. Both objects presented similar behaviors, despite the differences in material properties. The computational model proposed by Equation (56) was used to fit the experimental data, and the resulting parameters were $c = 0.6$, $\delta = 2.0$ for the book and $c = 0.9642$, $\delta = 1.324$ for the metal slab.